minerals

MDPI

Article

Exploring Platinum Speciation with X-ray Absorption Spectroscopy under High-Energy Resolution Fluorescence Detection Mode

Clément Laskar [1,2,*], Elena F. Bazarkina [3,4,5], Maria A. Kokh [1,6,7], Jean-Louis Hazemann [3], Stéphane Foulon [8], Olivier Leynaud [3], Elsa Desmaele [9] and Gleb S. Pokrovski [1]

1 Géosciences Environnement Toulouse (GET), UMR 5563, Centre National de la Recherche Scientifique (CNRS), Observatoire Midi-Pyrénées, Institut de Recherche pour le Développement (IRD), Université Toulouse III Paul Sabatier (UPS), Centre National d'Etudes Spatiales (CNES), 14, Avenue Edouard Belin, 31400 Toulouse, France
2 Laboratoire de Génie Chimique (LGC), Université de Toulouse, CNRS UMR 5563, INP, UPS, 4, Allée Emile Monso, 31400 Toulouse, France
3 Institut Néel, UPR 2940 CNRS, Grenoble, France Université Grenoble Alpes, 25, Avenue des Martyrs, CEDEX 9, 38042 Grenoble, France
4 Institute of Resource Ecology, Helmholtz Zentrum Dresden-Rossendorf (HZDR), P.O. Box 510119, 01314 Dresden, Germany
5 The Rossendorf Beamline at ESRF, The European Synchrotron, CS40220, CEDEX 9, 38043 Grenoble, France
6 Institut für Geowissenschaften, Universität Potsdam, Campus Golm, Haus 27, Karl-Liebknecht-Str. 24-25, 14476 Potsdam, Germany
7 Institut für Mineralogie, Westfälische Wilhelms-Universität Münster, Corrensstrasse 24, 48149 Münster, Germany
8 Institut de Chimie de Toulouse (ICT), Université Toulouse III Paul Sabatier (UPS), CNRS UAR 2599, 118, Route de Narbonne, 31062 Toulouse, France
9 École Normale Supérieure—PSL Research University, Département de Chimie, Sorbonne Universités—UPMC Univ Paris 06, CNRS UMR 8640 PASTEUR, 24, Rue Lhomond, 75005 Paris, France
* Correspondence: clement.laskar@gmail.com

Abstract: Critical to interpreting platinum chemical speciation using X-ray absorption spectroscopy (XAS) is the availability of reference spectra of compounds with known Pt redox and coordination. Here we compare different techniques for Pt L_{III}-edge X-ray absorption near edge structure (XANES) and extended X-ray absorption fine structure (EXAFS) spectral regions for a large set of Pt-O-Cl-S reference compounds of known structures. The measurements were conducted in HERFD (high-energy resolution fluorescence detection, high-resolution or HR) mode, as well as in two conventional modes such as transmission (TR) and nominal-resolution total fluorescence yield (TFY or NR). Samples analyzed here included Pt^0 (TR), $Pt^{II}S$ (HR), $Pt^{IV}S_2$ (TR), $K_2Pt^{II}Cl_4$ (HR + TR), $K_2Pt^{IV}Cl_6$ (HR + TR), $Pt^{IV}O_2$ (HR + TR), $C_6H_{12}N_2O_4Pt^{II}$ (HR + TR), and aqueous solutions of $K_2Pt^{II}Cl_4$ and $H_2Pt^{IV}Cl_6$ (NR + TR), as well as $(NH_4)_2Pt^{IV}(S_5)_3$ (HR + TR). XANES spectra in HERFD mode offer a better energy resolution than in conventional modes, allowing a more accurate identification of Pt redox state and coordination geometry. EXAFS spectra in all three modes for a given compound yield identical within errors values of Pt-neighbor interatomic distances and mean square relative displacement (MSRD, σ^2) parameters. In contrast, both TR and NR spectra on the one hand and HR spectra on the other hand yield distinct amplitude reduction factor ($S_0{}^2$) values, 0.76 ± 0.04 and 0.99 ± 0.07 (1 standard error), respectively. This study contributes to the development of an open-access XAS database SSHADE.

Keywords: platinum; platinum sulfide; platinum disulfide; potassium tetrachloroplatinate; potassium hexachloroplatinate; platinum dioxide; carboplatin; mineral synthesis; XANES; EXAFS; amplitude reduction factor

Citation: Laskar, C.; Bazarkina, E.F.; Kokh, M.A.; Hazemann, J.-L.; Foulon, S.; Leynaud, O.; Desmaele, E.; Pokrovski, G.S. Exploring Platinum Speciation with X-ray Absorption Spectroscopy under High-Energy Resolution Fluorescence Detection Mode. *Minerals* **2022**, *12*, 1602. https://doi.org/10.3390/min12121602

Academic Editors: Donggao Zhao, Shui-Yuan Yang and Zhenyu Chen

Received: 27 October 2022
Accepted: 9 December 2022
Published: 13 December 2022

1. Introduction

Platinum forms a variety of minerals (e.g., native platinum, cooperite PtS, sudovikovite $PtSe_2$, sperrylite $PtAs_2$) and synthetic phases (e.g., PtO_2, cisplatin $Pt(NH_3)_2Cl_2$, carboplatin $C_6H_{12}N_2O_4Pt$, K_2PtCl_4, K_2PtCl_6) largely used in industry [1–3] and medicine [4–6]. In these solids, platinum commonly exists in three formal oxidation states (0, II, and IV; [7]), forming a variety of structures, from square-planar to dodecahedral (e.g., Figure 1). Platinum, being a trace metal in nature (0.8 ppb in the Earth's upper continental crust; [8]), also comes as isomorphic substitutions in major minerals (e.g., pyrite, chalcopyrite, pyrrhotite). In natural aqueous fluids and silicate/sulfide melts, platinum forms complexes with the major inorganic ligands (O/OH, Cl, S) [9–18]. Therefore, knowledge of the Pt redox state and detailed structural environment at the atomic scale in geological materials is required both for understanding the behavior of platinum in natural systems and optimizing its use in numerous technological applications.

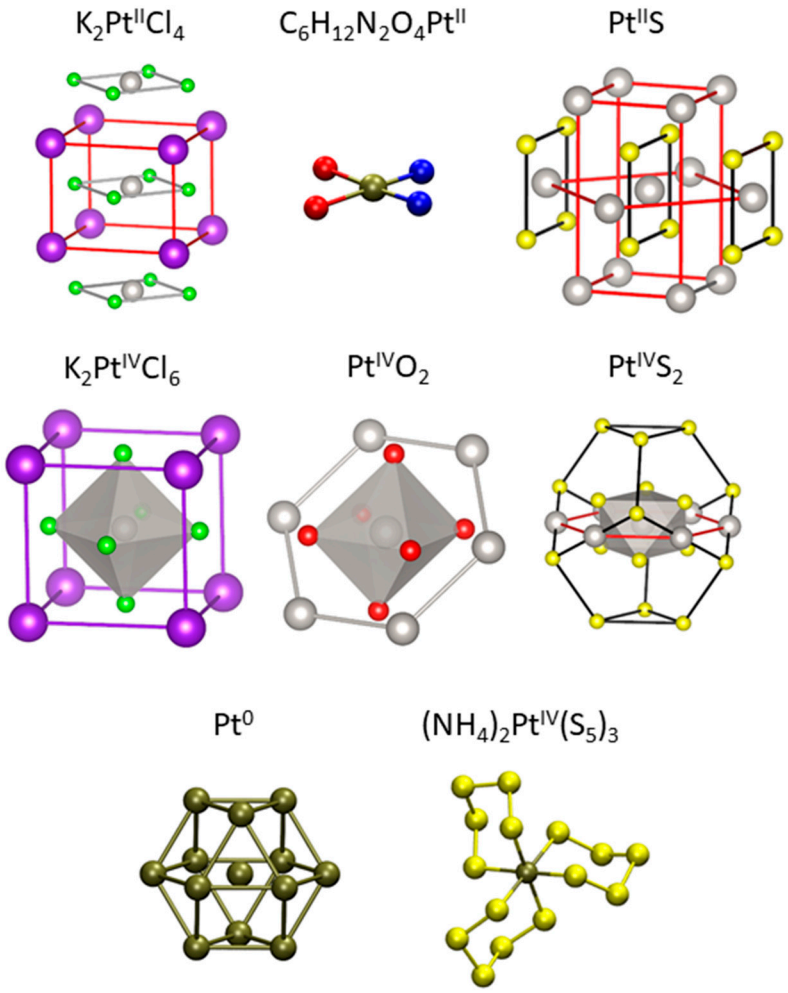

Figure 1. Ball-and-stick structural representation of the nearest coordination shells of the solid compounds investigated in this study. Atoms shown are those taken into account in the EXAFS modeling (Pt—grey, S—yellow, Cl—green, O—red, K—purple, N—blue). First shell shaded polyhedra and colored bonds were added for clarity. The Pt atom and the S atoms of the 3 cycles in the $Pt^{IV}(S_5)_3^{2-}$ ion adopt a chair-like conformation, with 6 S atoms in the 1st shell and 6 S atoms in the 2nd shell.

This knowledge can be provided by X-ray spectroscopy at synchrotron radiation facilities, which is the most direct probe of Pt coordination, oxidation state, and local atomic environment. X-ray absorption spectroscopy (XAS) can be recorded in transmission and in fluorescence mode as well. An XAS spectrum includes X-ray absorption near edge (XANES)

and extended X-ray absorption fine structure (EXAFS) parts. The XANES part provides information about the element oxidation state and coordination geometry. The EXAFS part, being complementary to XANES, helps to identify the ligands around the absorbing element and to quantify their numbers and interatomic distances in chemical complexes formed by the absorbing element in solid, gaseous, liquid, or aqueous phases [19–23]. When applied to low Pt concentrations, conventional fluorescence measurements using solid-state detectors have been widely used to study Pt in its different phases and complexes using both XANES and EXAFS analyses (e.g., [24–27]). However, conventional fluorescence- as well as transmission-mode XAS [16,28–30] are rather limited as to the discrimination between Pt^{II} and Pt^{IV}, or among different atomic neighbors (e.g., S vs. Cl, O vs. N) in similar types of solids (e.g., $Pt^{II}S$ vs. $Pt^{IV}S_2$) or aqueous complexes (e.g., $Pt(HS)_n$ vs. $PtCl_n$). Compared to conventional fluorescence, HERFD was commonly applied only to XANES analyses, for which it presents numerous benefits: (i) it enables a far better XANES shape definition and may reveal pre-edge and post-edge features that are poorly resolved (if detectable at all) in conventional mode (e.g., [31–36]); (ii) it is more sensitive to the presence of light elements whose presence affects HERFD-XANES spectra (e.g., H in Pt catalytic materials; [26]) and more discriminative for neighbors with close atomic numbers or monomeric vs. polymeric ligands of the same element (e.g., HS^- vs. S_3^-; [18,37]); (iii) it allows elimination of unwanted fluorescence signals from other elements with edges close to that of Pt [38], such as tungsten (W-L_{II} edge; 11,544 eV), gold (Au L_{III}-edge; 11,919 eV), arsenic (As-K edge; 11,867 eV), tantalum (Ta-L_I edge; 11,682 eV), or rhenium (Re-L_{II} edge; 11,959 eV). To better estimate the accuracy and limitations of the HERFD-EXAFS, especially for Pt-bearing complexes and materials cited above for which conventional XAS is not sensitive enough, additional studies are required. However, the studies on Pt compounds using HERFD-XAS have so far been mostly devoted to catalytic materials [39–50] and remain virtually non-existent for minerals and other geological samples [51]. Furthermore, a straightforward interpretation of HERFD-XAS data requires spectra of reference compounds with a known Pt atomic environment acquired at the same spectral resolution.

The goal of this study is to systematically analyze the XAS spectra of high-quality reference compounds of Pt solid phases of known crystal structures using both high-resolution (HR) and conventional XAS (transmission—TR, and nominal-resolution total fluorescence yield, TFY—NR) in order to compare both techniques and identify their advantages and limitations for studying Pt. The following solid references were analyzed in this study: platinum metal (Pt^0), platinum(II) sulfide ($Pt^{II}S$), platinum(IV) disulfide ($Pt^{IV}S_2$), potassium tetrachloroplatinate (II) ($K_2Pt^{II}Cl_4$), potassium hexachloroplatinate (IV) ($K_2Pt^{IV}Cl_6$), platinum (IV) dioxide ($Pt^{IV}O_2$), and diamine (cyclobutane-1,1-dicarboxylato (2-)-O,O′) platinum (II) ($C_6H_{12}N_2O_4Pt^{II}$). Substantial work was made to synthesize pure references of $Pt^{II}S$ and $Pt^{IV}S_2$ in this study. Additionally, ammonium tris(pentasulfido) platinum(IV), $(NH_4)_2Pt^{IV}(S_5)_3$), representative of Pt^{IV} in a sulfur-coordinated first and second shell environment, was also synthetized and thoroughly characterized to be examined by XAS using the approaches established on the reference compounds. In particular, we attempted to assess the potential of HR-XAS in detecting second shell sulfur atoms in polysulfide complexes that may be important carriers of chalcophile metals in hydrothermal fluids [18,52–54]. The Pt-S solids synthesized and analyzed in this study are particularly important for HERFD-XAS analyses of Pt in natural sulfide minerals of hydrothermal and magmatic origin that represent the PGE major economic resource (e.g., [55–58]). Our results provide a systematic assessment of the advantages and limitations of HR-XAS for the study of platinum species and contribute to spectroscopic databases of Pt compounds such as the SSHADE database [59] that will help future synchrotron-based studies of this economically critical metal. SSHADE is an open-access spectroscopy database infrastructure (https://www.sshade.eu/ (accessed on 9 December 2022)) created in 2018 and currently gathering 5230 spectra (including XAS, Raman, and FTIR), with 580 XAS spectra for natural and synthetic solids and solutions, acquired and thoroughly described with an exhaustive

set of metadata by 20 different groups of users of BM16 and BM30 CRG beamlines at the ESRF.

2. Materials and Methods

2.1. Experimental Samples

2.1.1. Origin of the Investigated Compounds and Solutions

The following Pt-bearing solids were purchased from chemical suppliers and used without further treatment: potassium platinum (II) chloride (K_2PtCl_4, Pt 46.0%, trace metal basis 99.9%, serial number #61601032, ThermoFisher), potassium platinum (IV) chloride (K_2PtCl_6, Pt 39.6%, #61600659, ThermoFisher, Kandel, Germany), platinum (IV) dioxide (PtO_2, Pt 84.4% min, trace metal basis >99.95%, #R12B020, ThermoFisher, Kandel, Germany), platinum (IV) disulfide (PtS_2, Pt 74.8% min, #R22D024, ThermoFisher, Kandel, Germany), and diamine (cyclobutane-1,1-dicarboxylato(2-)-O,O′) platinum "carboplatin" ($C_6H_{12}N_2O_4Pt$, purity ≥95%, Cayman Chemical, Ann Arbor, MI, USA). Powder X-ray diffraction (XRD) patterns of K_2PtCl_4, K_2PtCl_6, and PtO_2 corresponded to the pure crystalline compounds, but that of PtS_2 was highly problematic (see below). Therefore, the PtS_2 solid along with PtS and $(NH_4)_2Pt(S_5)_3$ that were commercially unavailable, has been synthesized in this study. The following chemicals were used: platinum black powder (≤20 µm, ≥99.97%, surface area ≥25 m^2/g, Aldrich, Saint-Louis, MO, USA), platinum metal powder (>99.9%, 325 mesh, ThermoFisher, Kandel, Germany), aqueous diammonium sulfide solution ($(NH_4)_2S$, 40–44 wt%), sulfur powder (99.98%, Aldrich, Saint-Louis, MO, USA), chloroplatinic acid (H_2PtCl_6, 0.38 wt% Pt, Aldrich, Saint-Louis, MO, USA), toluene, methanol, N,N-dimethylformamide (DMF). The synthesis and characterization of the platinum sulfide solids are described in the following subsections. Aqueous solutions of $K_2Pt^{II}Cl_4$ (0.015 mol/kg soln Pt, hereafter K_2PtCl_4 aq) and $H_2Pt^{IV}Cl_6$ (0.007 mol/kg soln Pt, hereafter H_2PtCl_6 aq) were prepared by dissolution, respectively, of $K_2PtCl_{4(s)}$ and H_2PtCl_6 in water, and adding NaCl and HCl to stabilize Pt in solution. Table 1 summarizes the investigated samples, their origin, and the XAS acquisition modes applied.

Table 1. The solid and aqueous reference compounds analyzed by XAS in this study.

Solid	Origin	Beamline Used	Mode	Concentrations, wt% Pt
Pt metal	GoodFellow (10 µm thickness, 99.95%)	FAME	TR	>99.9
		FAME-UHD	TR	>99.9
PtS-h	This study (hydrothermal)	FAME-UHD	HR + TR	1.1
PtS-s	This study (solid-state)	FAME	TR	3.6
PtS_2-s	This study (solid-state)	FAME	TR	3.5
PtS_2-c *	ThermoFisher (not pure)	FAME-UHD	HR + TR	1.5
$(NH_4)_2Pt^{IV}(S_5)_3$	This study	FAME-UHD	HR + TR	1.4
K_2PtCl_4-a	ThermoFisher (99.9%)	FAME-UHD	HR + TR	0.9
K_2PtCl_4-b	ThermoFisher (99.9%)	FAME	TR	3.1
K_2PtCl_4 aq	This study	FAME	NR + TR	0.3
K_2PtCl_6-a	ThermoFisher	FAME-UHD	HR + TR	0.9
K_2PtCl_6-b	ThermoFisher	FAME	TR	3.0
H_2PtCl_6 aq	This study	FAME	NR + TR	0.1
$C_6H_{12}N_2O_4Pt$	Cayman Chemical (≥95%)	FAME-UHD	HR + TR	1.1
PtO_2-a	ThermoFisher (99.95%)	FAME-UHD	HR + TR	1.1
PtO_2-b	ThermoFisher (99.95%)	FAME	TR	3.7

* mixture of amorphous PtS and elementary sulfur; wt%, weight percent.

2.1.2. Synthesis of PtS and PtS_2

The platinum(II) sulfide (PtS) solid has been reported to be synthesized either hydrothermally at acidic pH at 450 °C from a mixture of elemental Pt and S [11,15] or by the solid-state method in silica tubes at 750 °C [60] and 1000 °C [10]. Platinum (IV) disulfide (PtS_2) has been hydrothermally synthesized at ~100 °C at neutral pH [11], in solid-state in silica tubes at 800 °C [61] and 1000 °C [10], and in a flow of H_2S with $(NH_4)_2PtCl_6$ as the reactant at 130 °C [62]. In this study, we used both hydrothermal and solid-state syntheses. Hydrothermal PtS (hereafter PtS-h) was obtained from stoichiometric quantities

of platinum black powder and sulfur powder in 0.1 mol/L NaOH in deionized water placed in a titanium (grade alloy VT-8) reactor at 450 ± 5 °C and 500 ± 20 bar for 11 days [15]. X-ray diffraction patterns of the solid show a high crystallinity of the corresponding pure phase (Figure A1d). Solid-state PtS (hereafter PtS-s) was obtained by annealing of a slightly non-stoichiometric mixture of elemental platinum and sulfur powders (S:Pt ratio of 1.1 to compensate for the partial sulfur loss in the vapor phase; [63]). The mixture was compacted at the bottom of a fused silica tube sealed under argon atmosphere and placed in a horizontal furnace at 750 °C for 10 days. After the experiment, the tube was cooled down to room temperature at a rate of 100 °C/h by keeping it in the furnace switched off. Platinum disulfide PtS_2 was synthesized by the same solid-state method (with a S:Pt ratio of 2.3:1.0). Note that, compared to previous studies [10,61], our chosen temperature is lower, thereby significantly reducing the risk of the silica tube break due to the pressure of S_2 (gas) that strongly increases with increasing temperature (e.g., 28 bar at 750 °C versus 40 bar at 800 °C; [63]). Scanning electron microscopy (SEM) pictures of the obtained PtS and PtS_2, collected using a Tescan Vega 4 microscope in secondary electron mode, show small crystals (2–10 µm; Figure 2a,b). X-ray diffraction patterns of both solids show a high crystallinity of the corresponding phase (Figure A1b,c), and small amounts (10 ± 5%) of PtS_2 in the PtS solid. This impurity, as quantified by a Rietveld refinement (using a pseudo-Voigt profile function and a zero-shift displacement), is likely due to minor sulfur excess in the synthesis.

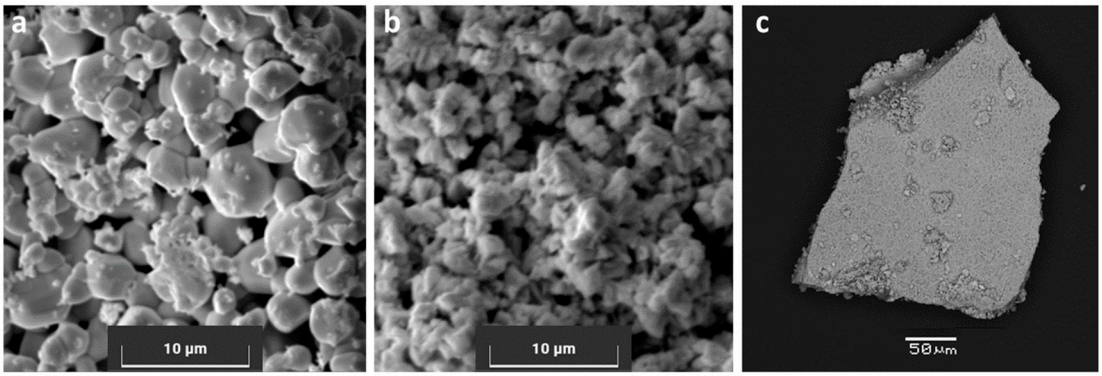

Figure 2. SEM photomicrographs (in secondary electron mode) of $Pt^{II}S$ (**a**), $Pt^{IV}S_2$ (**b**), and $(NH_4)_2Pt^{IV}(S_5)_3$ (**c**). The PtS grains have a tetrahedral shape. The PtS_2 grains are smaller and layered; they do not display clear geometric shapes. The $(NH_4)_2Pt^{IV}(S_5)_3$ solid is an agglomerate of amorphous particles.

2.1.3. Commercial PtS_2

Commercially purchased platinum disulfide (see Section 2.1.1, hereafter PtS_2-c) was analyzed to check for its purity and crystallinity. It was found to exhibit the XRD pattern of an amorphous compound (Figure A1e) that looked suspiciously similar to the XRD pattern of amorphous sulfur [64]. The S:Pt ratio in this solid was determined by dissolution: 25 mg of PtS_2-c powder was dispersed in 5 mL of hot aqua regia (~70 °C; 2/3 HCl of 37 wt% + 1/3 HNO_3 of 69 wt%) for 3 h to achieve complete dissolution; then aqua regia was evaporated to a wet residue (<0.3 g) and diluted with an acidic aqueous solution (HCl 0.5 wt% − HNO_3 1.5 wt%), which was analyzed by Inductively Coupled Plasma Optical Emission Spectrometry (ICP-OES). The obtained S:Pt molal concentration ratio of 3 (vs. the stoichiometric ratio 2) clearly indicates that the "PtS_2" solid as claimed by the chemical company is in reality highly non-stoichiometric and likely consists of amorphous PtS with a large fraction of elemental sulfur.

2.1.4. Synthesis of $(NH_4)_2Pt^{IV}(S_5)_3$

The synthesis of the $(NH_4)_2Pt^{IV}(S_5)_3$ solid has been a subject of several studies using different protocols of variable complexity [65–68]. We have adopted the method of [68],

which is the most straightforward way of avoiding the use of highly toxic carbon disulfide CS_2. Our synthesis included the following steps. First, polysulfide anions were generated by saturating 5 mL of $(NH_4)_2S$ (40–44 wt%) aqueous solution with an excess of powder sulfur (of the 3 g of sulfur added, ~2 g were dissolved after 10–15 min). This sulfur-saturated solution contains a mixture of polysulfides among which the pentasulfide anion S_5^{2-} is the most abundant one [69]. The remaining solid sulfur was removed by filtration. Then, to the produced polysulfide solution, 10 mL of H_2PtCl_6 (0.0198 mol/kg soln) aqueous solution was added dropwise while vigorously stirring. Assuming mainly the pentasulfide ion was formed, approximately 100 moles of S_5^{2-} were available per 1 mole of platinum. The resulting mixture was quickly filtered and the filtrate was stored at 5 °C for 24 h. The solution was then centrifuged (3800 rpm for 15 min). Finally, the obtained brick-red to maroon-colored precipitate was washed twice with a small amount of cold water and purified three times with a few mL of methanol (CH_3OH) and toluene (C_7H_8) to remove the remaining sulfur. The obtained product was re-dispersed in 10 mL of N,N-dimethylformamide (DMF). The DMF solvent was evaporated for 1 day at 70 °C, while letting the $(NH_4)_2Pt^{IV}(S_5)_3$ precipitate in the condensed phase to avoid its potential volatilization or decomposition that may occur when using more elevated temperatures (>100–150 °C; [70]).

Scanning electron microscopy (SEM) coupled with energy dispersive X-ray spectroscopy (EDS) was also used to quantify the amount of sulfur and platinum in the synthesized solid (Figure 2c) using a Bruker Nano GmbH microscope with a Quantax EDS unit. An atomic ratio of S:Pt = 14.4 was found, which is close to the stoichiometric S:Pt ratio of 15.0 in this compound. The X-ray diffraction (XRD) analysis of the produced precipitate showed an amorphous pattern (Figure A1a). The XRD pattern shows the presence of crystalline impurities of ammonium sulfate, $(NH_4)_2SO_4$, and elemental sulfur (Figure A1a). An infrared spectrum for this powder sample was collected using a Nicolet 6700 Thermoscientific spectrometer, in the range 100–600 cm^{-1}, with a resolution of 8 cm^{-1}, and an attenuated total reflectance (ATR) iTX^{TM} for a total of 16 scans (Figure A2a). Despite the small amount of available solid and the resulting weak signal, the spectrum shows 4 peaks (3 peaks at 551, 487, and 462 cm^{-1} and a broad feature at ~278 cm^{-1}; Table 2), which are in decent agreement with those reported by [65] for the analogous crystalline compound (568 cm^{-1} for an NH_4^+ vibration mode, 490 and 450 cm^{-1} for the S-S mode, and a shoulder at 294 cm^{-1} for the Pt-S mode). A UV-Vis spectrum of $(NH_4)_2Pt^{IV}(S_5)_3$ aqueous solution was collected using a Specord S600 spectrophotometer at 25 ± 1 °C in the range 184–1020 nm with a 0.5 nm resolution and an integration time of 60 ms (Figure A2b, Table 2). The two identified peaks at 290 and 385 nm are similar both in their energy position and amplitude ratio (1.2) to those reported by Wickenden and Krause (1969) [65]. The obtained solid was analyzed as a sample by XAS using the approach established in this study on the Pt reference compounds.

Table 2. Major absorbance frequency positions in the far-infrared (IR) and the UV-visible spectrum of $(NH_4)_2Pt^{IV}(S_5)_3$ obtained in this study and its comparison with literature values.

Infrared	**Frequency, cm^{-1}**				
	278	461 w	487 w	551 s	This study
	286 s 294	450 w	490 w	568 b	[65]
	Wavelength, nm				
UV-visible	<200	290	385	This study	
	<190	290	390	[65]	

s—strong; b—broad; w—weak.

2.2. X-ray Absorption Spectroscopy (XAS)

2.2.1. Acquisition Setup

The X-ray absorption spectra were recorded at the Pt L_{III}-edge (~11,564 eV) at beamlines BM16-FAME-UHD [38] and BM30b-FAME [71] of the European Synchrotron Radiation

Facility (ESRF), Grenoble, France. Both beamlines have the same X-ray optics setup, with a Si (220) double-crystal monochromator with sagittal focusing for choosing the energy of X-rays delivered from a bending magnet, and two Rh-coated mirrors for harmonic rejection and vertical focusing, yielding a beam spot on the sample of 200 × 300 and 200 × 200 μm^2 (full width at half maximum, FWHM) at FAME and FAME-UHD, respectively. Both beamlines also use the same setup for acquisition in transmission mode, consisting of silicon diodes collecting scattered radiation from a Kapton foil placed in the incident and transmitted X-ray beam. The differences between the beamlines are in the fluorescence acquisition mode. At FAME, a solid-state (SS) multi-element detector is placed in the right-angle geometry to the incident beam (Canberra solid-state 13-element germanium detector). The dead time for all samples was around 2%. At such a dead time value, the signal is linear and there is no need for dead time correction. The dead time was not registered during scan acquisition, but the distance between the fluorescence detector and each sample was optimized to always remain within the linear part of fluorescence signal acquisition. At FAME-UHD, a high-energy resolution fluorescence detection (HERFD) setup is used [72], with a recently developed crystal analyzer spectrometer [73]. For Pt L_{III}-edge HERFD-XANES measurements, the spectrometer was tuned to the maximum $L\alpha_1$ (9.442 keV) X-ray emission line using the (660) reflection of a Ge (220) analyzer at a Bragg angle of 80°. Photons diffracted by the crystal analyzers were collected using a silicon drift mono-element detector (SDD).

The difference in energy resolution of TFY and HERFD is due to different widths of the energy levels involved in the absorption process. In conventional XAS, for an L_{III} absorption edge, the final state has a $2p_{3/2}$ core hole. In HERFD-XAS, the $L\alpha_1$ fluorescence line corresponds to the 3d to $2p_{3/2}$ electronic transition with a shorter core-hole lifetime. Fundamentally, the improvement in the HERFD-XANES spectral resolution compared to conventional spectra is a direct consequence of the difference between these final-state widths [31]. Because the energy resolution of the incident beam (beamline resolution) is always better than the energy bandwidth of the final state, the intensity in HERFD increase due to the transition will occur in a narrower energy range [31]. For Pt, the apparent core-hole lifetime broadening of the HERFD $L\alpha_1$ measurement is only 1.94 eV, whereas for the TFY and transmission, the core-hole broadening is 5.39 eV [38]. Please note that the resolution of the monochromator (0.65 eV; [38]) and the emission spectrometer (0.65 ± 0.05 eV as measured at the elastic peak of the $L\alpha_1$ Pt fluorescence line) are both below the apparent core-hole lifetime broadening (1.94 eV). As a result, the apparent core-hole lifetime broadening is the main factor determining the energy resolution of Pt HERFD spectra. In practice, due to selective filtering of the Pt fluorescence line by the crystal analyzers, the apparent energy resolution of HERFD spectra compared to conventional resolution provided by the SS detector is 1–2 eV versus >~5 eV [38].

At both beamlines, the energy calibration of each scan was achieved using a 25 μm Pt metal foil recorded in transmission mode whose L_{III}-edge energy was set to 11,564.0 eV as the maximum of the spectrum first derivative. The acquisition time for each XAS scan was ~40 min at both beamlines. For fluorescence measurements, the solids were diluted with boron nitride (BN) powder to have concentrations close to 0.5–1.5 wt% Pt in the sample both on FAME and FAME-UHD, well below the potential saturation level of the fluorescence detector (>5 wt%) and possible self-absorption effects (>2–3 wt%). The absence of self-absorption issues was carefully checked using the Athena software corrections as a well as by direct comparisons of the white-line intensities between conventional fluorescence and transmission spectra that were always identical. Powders were pressed in 5 mm diameter pellets and affixed to a sample holder. Aqueous solutions (K_2PtCl_4 aq, H_2PtCl_6 aq) were placed in the glassy-carbon inner cell of the hydrothermal apparatus developed at the Néel Institute ([74], see also Pokrovski et al., 2006 [75] for details). The spectra of the solid references were recorded at ambient conditions (25 °C, 1 bar), whereas those of aqueous solutions at 30 °C and ~600 bar to avoid potential beam-induced phenomena such as the formation of air bubbles common at ambient pressure.

2.2.2. EXAFS Spectra Modeling

The acquired XAS spectra[1] were analyzed using the Athena and Artemis programs [76], based on the IFFEFIT program [77], and following previously established protocols (e.g., [78]), according to the EXAFS function $\chi(k)$:

$$\chi(k) = S_0^2 \sum_{\text{shell i}} \frac{N_i A_i(k)}{kR_i^2} e^{\frac{-2R_i}{\lambda(k)}} \sin(2kR_i + \Phi_i(k)) e^{-2k^2\sigma_i{}^2} \quad (1)$$

where $S_0{}^2$ is the amplitude reduction factor, N_i is the coordination number in shell i, A_i is the backscattering amplitude, R_i is the interatomic distance, $\Phi_i(k)$ is a phase shift, and σ_i^2 is the mean square relative displacement (MSRD, so-called Debye–Waller factor). Spectra were normalized to the absorption edge height, and atomic background subtracted. Care was taken to process the spectra as consistently as possible, and to evaluate the effect of the different Athena tuning parameters for atomic background subtraction. This effect was checked by fits (see below) of EXAFS spectra extracted using different Athena parameters but was found to be very minor. Therefore, the following parameters have been chosen here for consistency, which are also in agreement with common EXAFS extraction recommendations (The Athena Users' Guide, [76,79]). The k-weight of the background polynome spline was chosen at 2 for all solids and at 1 for aqueous solutions, with a normalization order of 3 for all samples. The spline ranges in k and E were 0–14 $Å^{-1}$ and 0–740 eV (where 0 is the relative position of the absorption edge), respectively. The normalization ranges were from −115 to −30 eV for the pre-edge and from 150 to 730 eV for the post-edge. The E_0 parameter was chosen for all samples as the energy of the first maximum of the first derivative of μ(E) (Table A1). The frequency cutoff of the background, determined by the Rbkg parameter, was set to a value of 1.2 Å, which was found to be the most optimal for all samples because it provided Fourier transforms (FTs) clean from unphysical low-distance features while not affecting the higher-distance tail of the nearest neighbor shell, in particular for PtO_2 and $C_6H_{12}N_2O_4Pt$ compounds. An FT was applied to extract the frequency-dependent contributions from the backscattering atoms, using a Kaiser–Bessel window with a dk value of 3.0. Exploitable k-ranges of our EXAFS spectra were between 3–11 $Å^{-1}$ and 3–13 $Å^{-1}$, depending of the signal-to-noise ratios (S/N), with neither influence on $S_0{}^2$ values, nor on other EXAFS structural parameters, within their respective uncertainties.

Least-square EXAFS fits were performed in R-space on both real and imaginary parts of FT to obtain the structural information. In addition, a non-structural parameter, Δe, accounts for energy shift between experimental spectrum and FEFF calculations (FEFF6 ab initio code integrated in the Artemis program; [80]) that were used to calculate the amplitude and phase electron scattering factors for neighboring atoms. To derive $S_0{}^2$ from the spectra of well-known compounds, the coordination numbers N were fixed in the fit to the crystallographic values for each Pt-bearing compound. Fits were performed with k-weighting of 1, 2, and 3 to diminish correlations between ($N \times S_0{}^2$) and σ^2, and R and Δe, and to improve fit robustness [76]. The uncertainties of the derived structural parameters reported by the Artemis program were further assessed by comparing fits of the same EXAFS spectrum with different numbers of independent points (defined by the fitted k and R-ranges and the S/N ratio) and variables (by setting, constraining, or releasing some of them). The correlations intrinsic between specific EXAFS parameters (such as $S_0{}^2$ or N vs. σ^2, and R vs. Δe) have been carefully examined and their effect on the $S_0{}^2$ and R values assessed (see below). The uncertainties reported in this study typically correspond to 1 standard error (1 SE). The multiple scattering (MS) contributions were considered for all samples and, except for Pt metal, the only significant contribution was the forward through absorber linear scattering. However, because the EXAFS signal is in most cases strongly dominated by the first shell single scattering, MS contributions had almost negligible effect on the determination of $S_0{}^2$.

3. Results

3.1. XANES Results

It can be seen in Figure 3a and Table A1 that the XANES spectrum of the $K_2Pt^{II}Cl_4$ solid has a white-line energy 0.6 eV lower than $Pt^{II}S$, which is also in agreement with previous studies [16,28,29]. The Pt^{IV} hexa-coordinated compounds ($K_2Pt^{IV}Cl_6$ and $Pt^{IV}O_2$) have distinctly higher white-line amplitudes (by a factor of 2 to 3) and energy positions of white-line maximum (by 1 to 2 eV) than their Pt^{II} square-planar counterparts ($K_2Pt^{II}Cl_4$, $Pt^{II}S$), in good agreement with the general tendencies for metal coordination and oxidation state observed in XANES spectra in previous studies, e.g., [81]. The differences among the Pt^{IV}-S and Pt^{II}-S solids are revealed both in HR and TR modes (Figures 3b and A3), with a $Pt^{II}S$ white-line amplitude and energy position distinctly lower than those of $Pt^{IV}S_2$. Platinum disulfide of commercial origin (PtS_2-c) presents a spectrum in between those of $Pt^{II}S$ and crystalline $Pt^{IV}S_2$ (Figure A3b), illustrating its impure composition, which should include some $Pt^{II}S$. Aqueous solutions of K_2PtCl_4 and H_2PtCl_6 show similar normalized XANES spectra as their respective solid references K_2PtCl_4 and K_2PtCl_6, both in TR and NR modes, illustrating the spectral similarity between the two conventional acquisition modes (Figure A4).

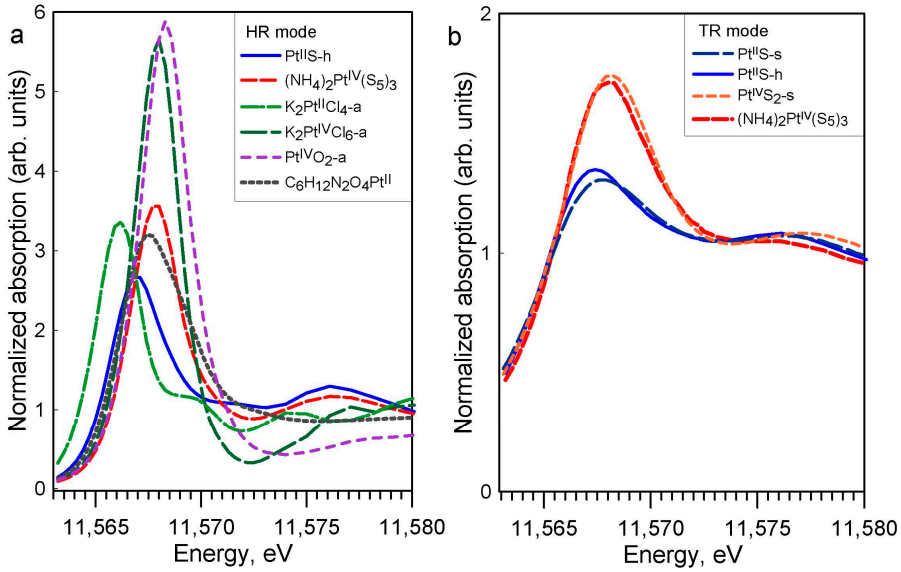

Figure 3. (**a**) Normalized Pt L_{III}-edge XANES spectra in high-resolution (HR) mode for the indicated compounds investigated in this study at 25 °C and 1 bar. (**b**) Normalized Pt L_{III}-edge XANES spectra in TR mode for Pt^{II}S-h, $(NH_4)_2Pt^{IV}(S_5)_3$, Pt^{II}S-s, and $Pt^{IV}S_2$-s.

The Pt^{IV} hexa-coordinated compound ($(NH_4)_2Pt^{IV}(S_5)_3$) has a similar white-line amplitude and energy position of the white-line maximum as the other Pt^{IV} references investigated here (Figure 3a). Both $(NH_4)_2Pt^{IV}(S_5)_3$ and $Pt^{IV}S_2$ have very similar white-line shapes, positions, and amplitudes (Figure 3b), demonstrating that their XANES signals are largely dominated by a similar first shell Pt-S_6 clusters (Figure 1). Therefore, $(NH_4)_2Pt^{IV}(S_5)_3$ may also serve as a Pt^{IV}-S XANES reference for sulfide-bearing minerals and fluids. The presence of a second shell of sulfur atoms has no visual impact on the XANES spectra in HR-fluorescence mode, which show only one wide post-edge peak right to the white line (Figure A3a). The presence of more distant shells (Pt-Pt and Pt-S_2) is not directly detectable by XANES and would require more advanced ab initio modelling of XANES spectra, e.g., [18,36], which is beyond the subject of our exploratory study.

The HR-XANES acquisition mode offers a gain in resolution for the white-line compared to nominal-resolution XANES (Figures 4 and A5 and Table A1). This gain allows a more precise determination (±0.3 eV) of the white-line maximum energy position. This gain enables, for example, a more accurate distinction between the Pt^{II} and Pt^{IV} redox

states in sulfide and chloride solids, which was difficult in nominal-resolution spectra in some previous studies, e.g., [28,29]. The HR mode also results in a significant increase in amplitude and decrease in width of the post-edge XANES resonances, with each feature neatly emphasized (Figure 4), in particular for compounds having pronounced second shell signals evidenced by EXAFS (see below). These resolution improvements offered by HR mode allow more in-depth analyses of spectral differences among Pt-S and Pt-Cl compounds and better distinction between Pt redox states.

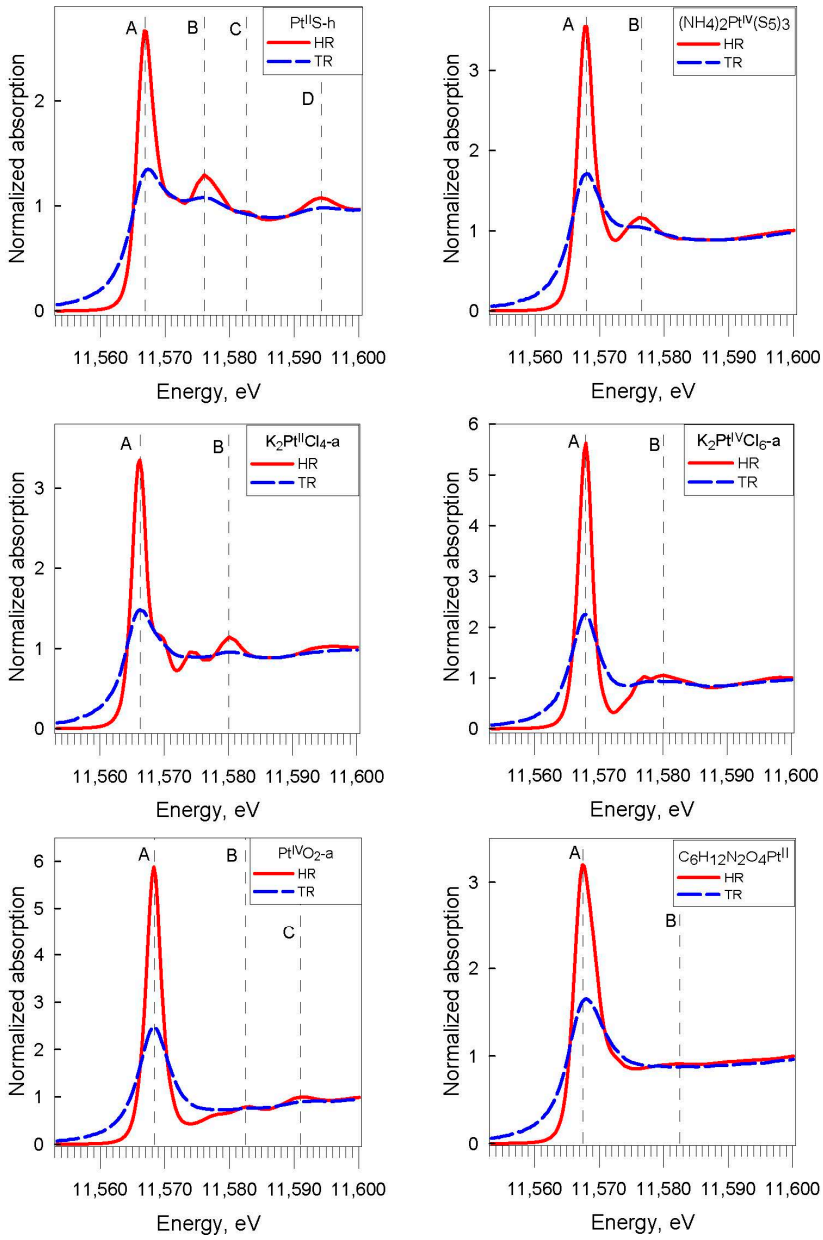

Figure 4. Normalized Pt L_{III}-edge XANES spectra of the indicated Pt solid phases investigated in this study at 25 °C and 1 bar. The spectacular improvement in high-resolution mode (HR, red), compared to transmission mode (TR, blue) enables precise determination of the white-line energy position and identification of post-edge spectral features. The major features are marked by vertical dashed lines with letters ((A) for the white-line and (B–D) for post-edge resonances). Uncertainty of the energy position is ±0.3 eV.

3.2. EXAFS Results

3.2.1. Reference Compounds

For all studied compounds (Pt^0, $Pt^{II}S$, $Pt^{IV}S_2$, $K_2Pt^{II}Cl_4$, $K_2Pt^{IV}Cl_6$, $Pt^{IV}O_2$, and $C_6H_{12}N_2O_4Pt^{II}$) whose spectra were acquired in HR (or NR) and TR modes, the EXAFS-derived interatomic distances are in good agreement with those from XRD crystallographic information (Table 3 and Figure A6), and the EXAFS features, which could be adequately fitted within the given S/N ratio, account for the nearest (and next-nearest when enough signal) coordination structures (Figure 5). Platinum–sulfur distances in the $Pt^{II}S$ solids derived by EXAFS fitting (Table 3) are in agreement within <0.01 Å with the crystallographic value (2.312 Å; [82]). For the $C_6H_{12}N_2O_4Pt^{II}$ solid, the EXAFS-derived Pt-N and Pt-O distances, 2.03 ± 0.02 Å and 2.36 ± 0.08 Å, respectively, (Table 3), are somewhat larger on average than the corresponding crystallographic values for cisplatin $Pt^{II}(NH_3)_2Cl_2$ with Pt-N and Pt-Cl distances of 1.995 Å and 2.317 Å, respectively [83]. More distant shells were too weak and composed of too light atoms to be properly fitted. Note that carboplatin is an unstable compound, rapidly degrading at ambient conditions, that brings additional noise to signal acquisition and may explain the differences found with the more accurate crystallographic values. In platinum chloride solids and solutions, Pt-Cl distances derived by EXAFS fitting (2.30–2.31 Å, Table 3) are in agreement within <0.01 Å with the crystallographic values [84,85]. For PtS_2 and PtO_2, the EXAFS-derived Pt-S_1 and Pt-O_1 first shell and Pt-S_2, Pt-O_2, and Pt-Pt_2 second shell distances are comparable with the crystallographic values within 0.08 Å for PtS_2 [86] and 0.05 Å for PtO_2 [87]. This agreement is believed to be reasonable in light of the complex second shell structures of these solids. Both fluorescence and transmission were recorded simultaneously to compare HR (or NR) and TR spectra from several samples (HR + TR, NR + TR; Table 1). Thus, as sample concentrations were optimized for fluorescence mode for these samples (0.5–1.5 wt% Pt, Table 1), requiring much lower Pt concentrations to avoid self-absorption and detector saturation effects [36], the S/N ratios of their transmission spectra were lower than those of their fluorescence spectra. However, these S/N differences, which are rather difficult to properly quantify in EXAFS, had only a very small impact on the resulting EXAFS-derived parameters (Table 3). Overall, all our samples yield the same interatomic distances as derived from transmission and fluorescence spectra. For example, for the most concentrated samples (~3 to 6 wt% Pt; PtS-s, K_2PtCl_4-b, K_2PtCl_6-b, PtO_2-b; Table 1) optimized for transmission measurements, both the interatomic distances and MSRD factors are similar with the same uncertainty magnitudes as those for samples specifically optimized for fluorescence mode (~1 wt% Pt; PtS-h, K_2PtCl_4-a, K_2PtCl_6-a, PtO_2-a; Table 1). In addition, no self-absorption effects were found in our fluorescence spectra (see Section 2.2.1). As a result, our data demonstrate good consistency in the EXAFS-derived structural parameters, which are the distances and MSRD factors, that are independent of the S/N ratio, Pt concentration, and acquisition mode. The major differences concern the amplitude reduction factor S_0^2, highlighted by the increased amplitude of the HR-EXAFS oscillation at low k compared to conventional EXAFS oscillations (Figure 6). In HR mode, the value of the S_0^2 parameter averaged over all investigated Pt references (Table 3) is 0.99 ± 0.07 (1 SE), whereas in TR and NR modes, this value is systematically lower on average, of 0.76 ± 0.04 (1 SE), as will be discussed in Section 4.2.

Table 3. Parameters of the Pt local atomic structure in the Pt solids and solutions obtained by fitting Pt L_{III}-edge EXAFS spectra and their comparison with crystallographic values.

		EXAFS Fit									Crystallographic Value [a]
Atom	**N**	**R, Å**	**$\sigma^2 \times 10^3$, Å^{-2}**	**Δe, eV**	***R*-Factor $\times 10^3$**	**S_0^2**	**R-Range, Å**	**k-Range, Å^{-1}**	**Number of Scans**	**Mode**	**R, Å**
Pt metal, FAME											
Pt	12	2.762 (4)	6 (1) [b]	8 (1)	18	0.75 (6)	1.2–6.0	3.0–12.0	7	TR	2.773
Pt	6	3.89 (2)	10 (5) [b]								3.922
Pt	24	4.8 (1)	9 (2) [b]								4.803
Pt_{fs}	24	5.525 [d]	24 (10)								
Pt_{dfs}	12	5.525 [d]	13 (3)								
Pt_{ot}	96	5.14 (4)	13 (10)								
Pt metal, FAME-UHD											
Pt	12	2.767 (3)	4.3 (6) [b]	8 (1)	9	0.79 (5)	1.2–6.0	3.0–12.0	13	TR	2.773
Pt	6	3.91 (1)	6 (2) [b]								3.922
Pt	24	4.807 (7)	7 (1) [b]								4.803
Pt_{fs}	24	5.525 [d]	22 (6)								
Pt_{dfs}	12	5.525 [d]	10 (2)								
Pt_{ot}	96	5.14 (3)	14 (10)								
PtS-h, FAME-UHD											
S	4	2.301 (8)	4 (1)	6 (1)	33	1.06 (12)	1.2–5.0	3.0–13.0	3	HR	2.312
Pt	4	3.47 (3)	9 (5)								3.470
Pt	8	3.89 (4)	9 (5)								3.918
S	8	4.10 (3)	8 (7)								4.169
S_{fwa}	4	4.61 [c]	7 [d]								
PtS-h, FAME-UHD											
S	4	2.303 (7)	3 (1)	10 (1)	29	0.85 (8)	1.2–5.0	3.0–13.0	3	TR	2.312
Pt	4	3.47 (3)	8 (5)								3.470
Pt	8	3.93 (3)	9 (5)								3.918
S	8	4.12 (4)	14 (10)								4.169
S_{fwa}	4	4.61 [c]	6 [d]								
PtS-s, FAME											
S	4	2.310 (4)	2.1 (8)	7 (1)	15	0.72 (4)	1.2–5.0	3.0–13.0	2	TR	2.312
Pt	4	3.47 (2)	8 (3)								3.470
Pt	8	3.92 (2)	7 (3)								3.918
S	8	4.13 (3)	8 (6)								4.169
S_{fwa}	4	4.62 [c]	12 (10)								
PtS_2-s, FAME											
S	6	2.385 (6)	2.4 (1.2)	9 (1)	28	0.77 (6)	1.2–5.0	3.0–13.0	2	TR	2.344
Pt	6	3.53 (1)	3 (2)								3.543
S	12	4.24 (2)	9 (5)								4.324
S_{fwa}	6	4.77 [c]	7 (7)								
K_2PtCl_4-a, FAME-UHD											
Cl	4	2.301 (7)	3 (1)	7 (1)	20	1.03 (10)	1.2–5.0	3.0–11.0	2	HR	2.308
K	8	4.06 (4)	6 (6)								4.078
Cl_{fwa}	4	4.61 [c]	5 (4)								
K_2PtCl_4-a, FAME-UHD											
Cl	4	2.293 (7)	1 (1)	9 (1)	42	0.8 (1)	1.2–5.0	3.0–11.0	2	TR	2.308
K	8	4.08 (3)	3 (1)								4.078
Cl_{fwa}	4	4.61 [c]	2 [d]								
K_2PtCl_4-b, FAME											
Cl	4	2.303 (5)	2 (1)	8 (1)	15	0.77 (1)	1.2–5.0	3.0–11.0	1	TR	2.308
K	8	4.09 (4)	23 (10)								4.078
Cl_{fwa}	4	4.61 [c]	5 (4)								
K_2PtCl_4 aq, FAME											
Cl	4	2.304 (5)	1 (1)	8 (1)	20	0.68 (5)	1.2–5.0	3.0–11.0	1	NR	2.308
Cl_{fwa}	4	4.61 [c]	17 [d]								

Table 3. *Cont.*

		EXAFS Fit									Crystallographic Value [a]
Atom	**N**	**R, Å**	**$\sigma^2 \times 10^3$, Å^{-2}**	**Δe, eV**	***R*-Factor $\times 10^3$**	**$S_0{}^2$**	**R-Range, Å**	**k-Range, Å^{-1}**	**Number of Scans**	**Mode**	**R, Å**
K_2PtCl_4 aq, FAME											
Cl	4	2.305 (6)	14 (14)	8 (1)	30	0.79 (7)	1.2–5.0	3.0–11.0	1	TR	2.308
Cl_{fwa}	4	4.61 [c]	28 [d]								
K_2PtCl_6-a, FAME-UHD											
Cl	6	2.311 (8)	3 (1)	6 (1)	23	1.0 (1)	1.2–5.0	3.0–11.0	2	HR	2.323
K	8	4.08 (6)	20 (10)								4.222
Cl_{fwa}	6	4.62 [c]	7 (7)								
K_2PtCl_6-a, FAME-UHD											
Cl	6	2.30 (1)	17 (15)	10 (2)	58	0.8 (1)	1.2–5.0	3.0–11.0	2	TR	2.323
K	8	4.2 (2)	40 (40)								4.222
Cl_{fwa}	6	4.61 [c]	33 [d]								
K_2PtCl_6-b, FAME											
Cl	6	2.312 (6)	1.5 (1.0)	8 (1)	16	0.78 (7)	1.2–5.0	3.0–11.0	1	TR	2.323
K	8	4.13 (6)	20 (15)								4.222
Cl_{fwa}	6	4.62 [c]	7 (7)								
H_2PtCl_6 aq, FAME											
Cl	6	2.314 (6)	1.2 (1.0)	8 (1)	20	0.71 (6)	1.2–5.0	3.0–11.0	2	NR	2.323
Cl_{fwa}	6	4.63 [c]	2 [d]								
H_2PtCl_6 aq, FAME											
Cl	6	2.315 (7)	1.2 [e]	9 (1)	44	0.78 (4)	1.2–5.0	3.0–11.0	2	TR	2.323
Cl_{fwa}	6	4.63 [c]	2.4 [d]								
$C_6H_{12}N_2O_4Pt$, FAME-UHD											
N	2	2.03 (2)	2 (1)	8 (3)	27	1.0 [f]	1.2–2.5	3.0–13.0	1	HR	1.995 [g]
O	2	2.36 (8)	23 (11)								2.317 [g]
PtO_2-a, FAME-UHD											
O	6	2.019 (6)	2 (1)	9 (1)	23	0.88 (6)	1.2–5.0	3.0–13.0	1	HR	2.070
Pt	6	3.104 (6)	2.4 (1.2)								3.100
O	12	3.68 (3)	9 (6)								3.598
O_{fwa}	6	4.04 [c]	5 [d]								
PtO_2-a, FAME-UHD											
O	6	2.010 (6)	1 (1)	12 (1)	27	0.74 (5)	1.2–5.0	3.0–13.0	1	TR	2.070
Pt	6	3.106 (6)	1.0 (8)								3.100
O	12	3.82 (5)	24 (15)								3.598
O_{fwa}	6	4.02 [c]	3 [d]								
PtO_2-b, FAME											
O	6	2.012 (5)	2 (1)	9 (1)	24	0.76 (5)	1.2–5.0	3.0–13.0	2	TR	2.070
Pt	6	3.100 (5)	3 (1)								3.100
O	12	3.67 (5)	10 (8)								3.598
O_{fwa}	6	4.02 [c]	4 [d]								

$S_0{}^2$ is the amplitude reduction factor determined by fixing the number of atoms N to their crystallographic values in the fit; uncertainties are calculated by the ARTEMIS program. All fits are performed in R-space. The number of variables (3–10) is always lower than the number of independent points (7–23) for all fits. The sample concentrations were optimized for fluorescence mode acquisition and not for transmission mode for all solids analyzed on FAME-UHD, except for Pt metal. Multiple scattering contributions: forward scattering (fs); double forward scattering; obtuse triangle (ot); forward through absorber (fwa) Pt-X-Pt-X-Pt (X = S or Cl or O). [a] Crystallographic references: Pt—[88]; PtS—[82]; PtS_2—[86]; K_2PtCl_6—[84]; K_2PtCl_4—[85]; PtO_2—[87]. [b] σ^2 values for Pt metal on FAME beamline are slightly higher than those on FAME-UHD because of the lower number of scans and, consequently, lower spectral S/N statistics at FAME. [c] R(X) is set to 2 × $R(X)_{1st\ shell}$ (X = S or Cl or O). [d] σ^2 (S) is set to 2 × σ^2 $(X)_{1st\ shell}$ (X = S or O). [e] σ^2 is set to that of H_2PtCl_6 aq in NR mode. [f] $S_0{}^2$ is set to that of PtS-h in HR mode. [g] Values are from $Pt^{II}(NH_3)_2Cl_2$ "cisplatin" crystallographic reference [89] because of the lack of data for $C_6H_{12}N_2O_4Pt^{II}$.

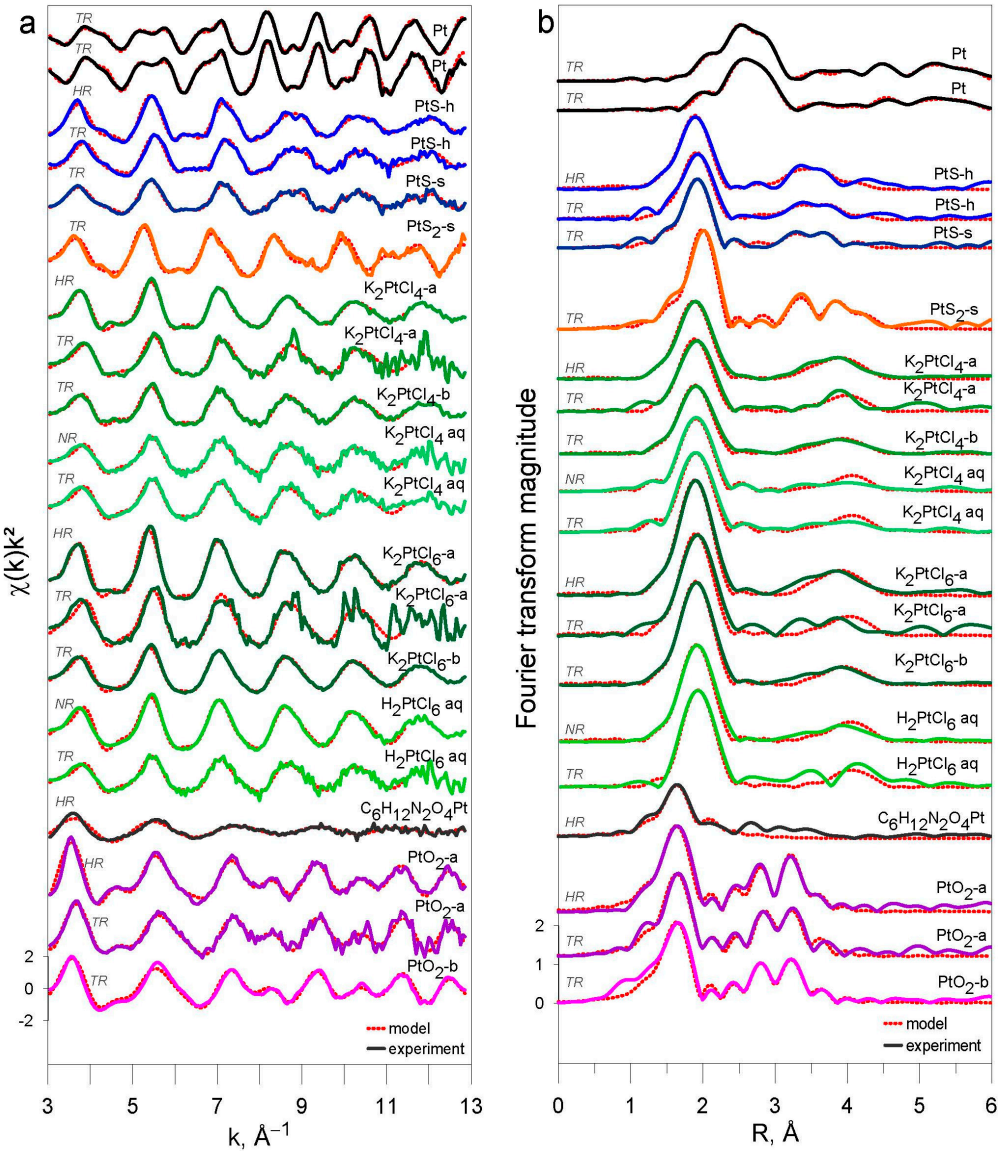

Figure 5. (**a**) k^2-weighted EXAFS spectra and (**b**) their corresponding Fourier transform magnitudes not corrected for phase shift of the investigated Pt-bearing references (see Table 1 for samples identity). Dotted curves are least-square fits to the experimental spectra shown by solid curves. HR—high-resolution fluorescence mode; NR—nominal-resolution fluorescence mode; TR—transmission mode. Experimental spectra of a given compound are colored for clarity, similarly to those in Figure 3. Labels are shown only for PtO_2-b for clarity; the Y-axis scale in both panels is identical for all spectra, which are shifted vertically for clarity.

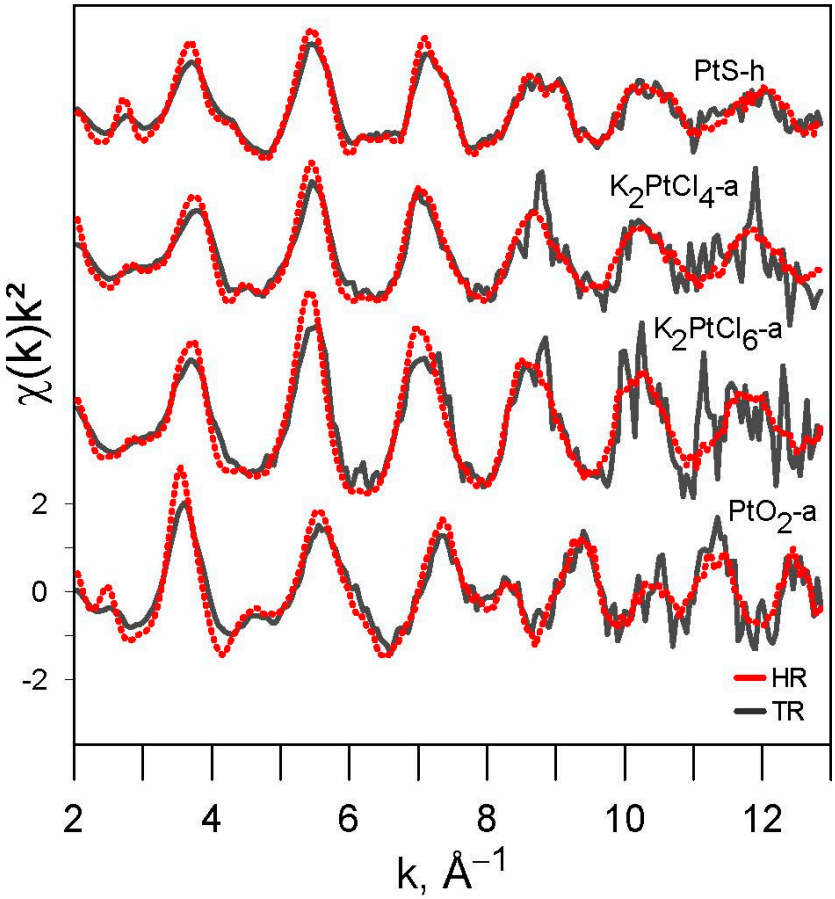

Figure 6. Comparison of k^2-weighted EXAFS spectra in transmission (TR) and HR-fluorescence (HR) modes of the investigated Pt-bearing references (see Table 1 for samples identity). Higher amplitudes at k < 8 $Å^{-1}$ are clearly apparent in the HR-EXAFS spectra.

3.2.2. $(NH_4)_2PtS_5$ Sample

The EXAFS fitting approach and the S_0^2 values derived above were validated on the $(NH_4)_2PtS_5$ sample. Modeling of EXAFS spectra of $(NH_4)_2Pt^{IV}(S_5)_3$ in HR and TR modes was performed with the two S_0^2 values determined from the other Pt references (see below and Table 4 and Figure 7). In both cases, the results are in good agreement with the known crystallographic structure of the solid [90]. The number of S atoms in the first shell is 5.7 ± 0.4 when S_0^2 is set to 0.99 in HR mode, and 5.8 ± 0.3 when S_0^2 is set to 0.76 in TR mode, which is within the uncertainties of nominal six S atoms from crystallographic data. Inversely, if S_0^2 is set to 0.76 in HR mode or to 0.99 in TR mode, for similar σ^2 values, the numbers of S atoms are either significantly overestimated (7.4 ± 0.5) or underestimated (4.5 ± 0.2), respectively. The number of S atoms in the second shell has larger uncertainties (±2–3), but yet converges to an average number of six atoms in all fits. The EXAFS-derived mean Pt-S_1 (1st shell) distance for $(NH_4)_2Pt^{IV}(S_5)_3$ is 2.370 ± 0.005 Å in HR mode and 2.366 ± 0.004 Å in TR mode, which is in the range of the XRD-derived values (2.358–2.436 Å; [90]). However, statistical resolution of our EXAFS spectra (0.16 Å, $\Delta R = \pi/2\Delta k$; e.g., [91,92]) does not allow the different Pt-S_1 crystallographic distances to be distinguished within the first shell (≤0.08 Å) reporting only a mean value (2.370 ± 0.005 Å in HR mode and 2.366 ± 0.004 Å in TR mode). The derived distance is significantly longer than those of other Pt-S compounds, such as PtS_2 (2.34 Å; [86]) and PtS (2.31 Å; [82]). The EXAFS-derived mean Pt-S_2 (2nd shell) distance, 3.56 ± 0.02 Å both in TR and HR modes, is coherent with the crystallographic value (3.39–3.81 Å; [90]). The multiple scattering contributions within the first shell S atoms are identical within uncertainties in both modes (4.78 ± 0.02 Å in HR and 4.76 ± 0.02 Å in TR mode). A wavelet transform analysis, based on the Continuous

Cauchy Wavelet Transform (CCWT; [93,94]), was performed for the $(NH_4)_2Pt^{IV}(S_5)_3$ (in HR and TR modes) and $Pt^{IV}S_2$-s solids (in TR mode), and confirmed the presence of both relatively light atoms (S_2) and MS in beyond-the-first shells of $(NH_4)_2Pt^{IV}(S_5)_3$, in contrast to $Pt^{IV}S_2$ whose second shell is dominated by heavy Pt atoms (Figure 8).

Table 4. Parameters of the Pt local atomic structure in the $(NH_4)_2Pt^{IV}(S_5)_3$ compound obtained by fitting Pt L_{III}-edge EXAFS spectra and the comparison with crystallographic values.

		EXAFS Fit						Crystallographic Value [a]	
Atom	**Mode**	**S_0^2**	**N**	**R, Å**	**$\sigma^2 \times 10^3$, Å^{-2}**	**Δe, eV**	***R*-Factor × 10^3**	**N**	**R, Å**
		$(NH_4)_2Pt^{IV}(S_5)_3$, FAME-UHD							
S_1 [b]	HR	0.99	5.7 (4)	2.370 (5)	6 (1)	8 (1)	12	6	2.358–2.436
S_2			7 (3)	3.56 (2)	20 (10)			6	3.39–3.81
S_{MS}			6 (3)	4.78 (2)	10 (10)			6	
S_1 [b]	TR	0.76	5.8 (3)	2.366 (4)	4 (1)	9 (1)	15	6	2.358–2.436
S_2			7 (2)	3.56 (2)	16 (9)			6	3.39–3.81
S_{MS}			5 (1)	4.76 (2)	8 [c]			6	

S_0^2 is the amplitude reduction factor set at the values of 0.76 and 0.99 for the HR and TR modes, respectively. R-ranges and k-ranges for all fits were, respectively, 1.2–5.0 Å and 3.0–13.0 Å^{-1}. Uncertainties are calculated by the ARTEMIS program and further evaluated by comparison of different fit models. All fits are performed in R-space. The number of variables (9–10) is always lower than the number of independent points (24) for all fits. Multiple scattering paths (MS) correspond to Pt-S_1-Pt-S_1-Pt. [a] values from [90]. [b] The potential distance resolution in our EXAFS fits for a k-range of 10 Å^{-1} is 0.16 Å [91,92], which does not allow discrimination of the different S distances ranging only over 0.08 Å in the distorted PtS_6 first shell octahedron according to the crystallographic data. [c] σ^2 (S_{MS}) is set to 2 × σ^2 (S_1).

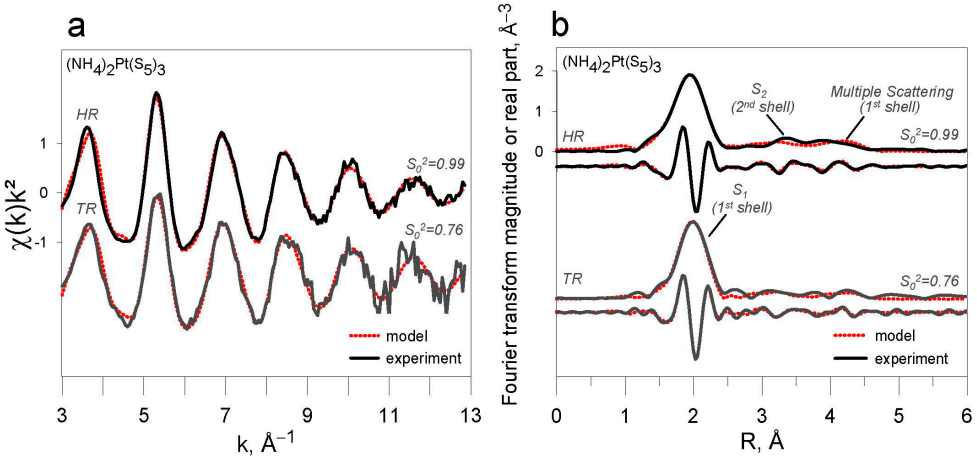

Figure 7. (**a**) k^2-weighted EXAFS spectra of the investigated $(NH_4)_2Pt^{IV}(S_5)_3$ compound and (**b**) their corresponding Fourier transform magnitude and real part (not corrected for phase shift, see Table 3 for phase-corrected distances). The S_0^2 values in the fits were set to 0.99 and 0.76 in HR and TR modes, respectively. Dotted curves are least-square fits to the experiment's spectra shown by solid lines. HR—high-resolution fluorescence mode; TR—transmission mode.

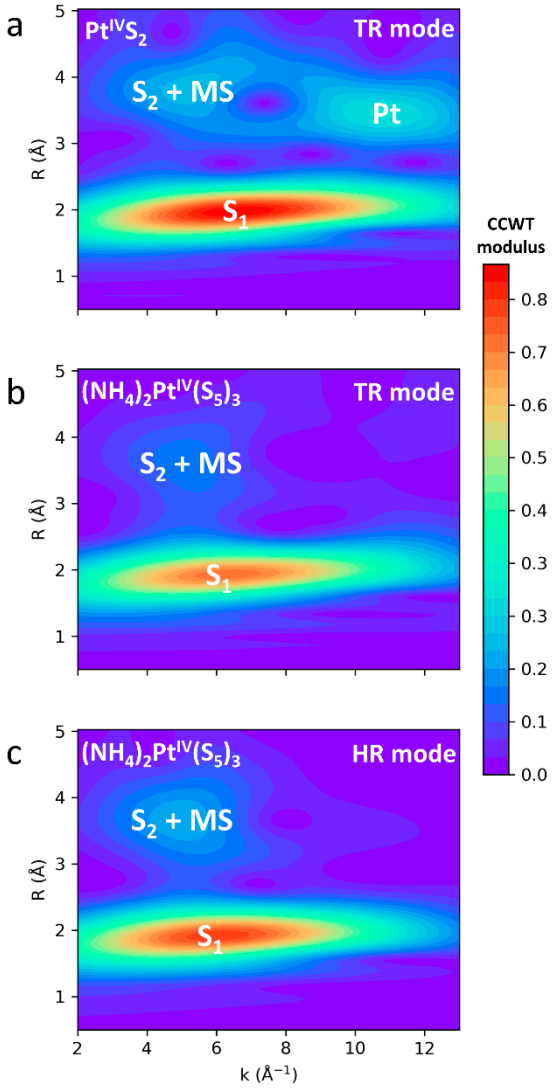

Figure 8. Wavelet analysis of k^2-weighted EXAFS spectra of $Pt^{IV}S_2$-s (**a**) and $(NH_4)_2Pt^{IV}(S_5)_3$ in TR mode (**b**) and HR mode (**c**), with the CCWT modulus showing the (k, R) localization of each EXAFS contribution (S_1 = 1st Pt shell, S_2 = 2nd Pt shell, MS = multiple scattering arising from the 1st Pt shell). No contributions from atoms heavier than S appear in $(NH_4)_2Pt^{IV}(S_5)_3$, either in TR or HR mode, in contrast with $Pt^{IV}S_2$-s showing strong contributions from the heavy Pt atoms in the 2nd shell.

4. Discussion

4.1. Resolution Improvement in HERFD Mode

Our results show that Pt L_{III}-edge XANES spectra acquired in HERFD mode (HR) show a significant gain both in the energy-position resolution and the shape and amplitude of white-line and post-absorption features, compared to conventional transmission (TR) or fluorescence (NR) modes, as has been already recognized in previous studies [39–41,44]. Therefore, the Pt^{II} and Pt^{IV} formal redox state and atomic coordination may be more clearly distinguished in Pt chloride- and sulfide-bearing systems in HR-XANES mode than in some previous works that used conventional acquisition modes [16,28,29,95]. This resolution improvement may add, in particular, more precision to the characterization of Pt-S and Pt-Cl complexes in hydrothermal fluids where a mixture of Pt^{IV} and Pt^{II} of different coordination may be expected, e.g., [18,96], as well as in natural mineral phases where Pt can be present in different coordination and oxidation states (e.g., Pt^{II} and Pt^{IV} in pyrite and pyrrhotite; [28,29]). It can be seen in Table A2 that the amplitude ratios between the main XANES resonances of the spectra of Pt^{II}-Cl versus Pt^{IV}-Cl, or Pt^{II}-S versus Pt^{IV}-S, types of compounds are significantly amplified in HR mode, allowing the use of these

ratios to quantify the fractions of the different complexes in a mixture. Until now, such an analysis was limited to Pt-O vs. Pt-Cl complexes [81], whose spectra have relatively strong contrasts in TR or NR modes.

4.2. Amplitude Reduction Factor (S_0^2)

We have not found any significant differences in the EXAFS spectra and the resulting fitted interatomic distances for the same compounds passed in HR and NR/TR modes (Table 3). Both beamlines provide identical S_0^2 values within errors in conventional modes (TR and NR), as illustrated here by Pt metal EXAFS fit results yielding 0.75 ± 0.06 on FAME and 0.79 ± 0.05 on FAME-UHD, similar to the values obtained at other synchrotrons in previous studies (0.82, [97]; 0.84 ± 0.03, [98]). Even though S_0^2 values in HR and NR/TR modes are all within the typical range of 0.65–1.10 reported for many elements at different beamlines (e.g., [99,100]), there is a systematic difference of >0.2 on average between the two sets of values (Figure 9). For example, Asakura et al. (2018) [97] reported the same gap with an S_0^2 value of 1.00 in HR mode versus 0.82 in NR mode from EXAFS fitting of platinum metal at Pt L_{III}-edge. Indeed, spectra in HR mode were reported to have larger amplitudes than in TR mode due to a smaller apparent core hole (e.g., [97,101]), yielding an increase in the amplitude of the EXAFS signal in the k-range 2–6 $Å^{-1}$ compared to the spectra in TR or NR modes (Figure 6). However, the disorder, represented by the mean square relative displacement, σ^2, is known to contribute to the EXAFS signal more significantly at higher k values (>8–10 $Å^{-1}$), and might also influence the determination of S_0^2. This effect is discussed below.

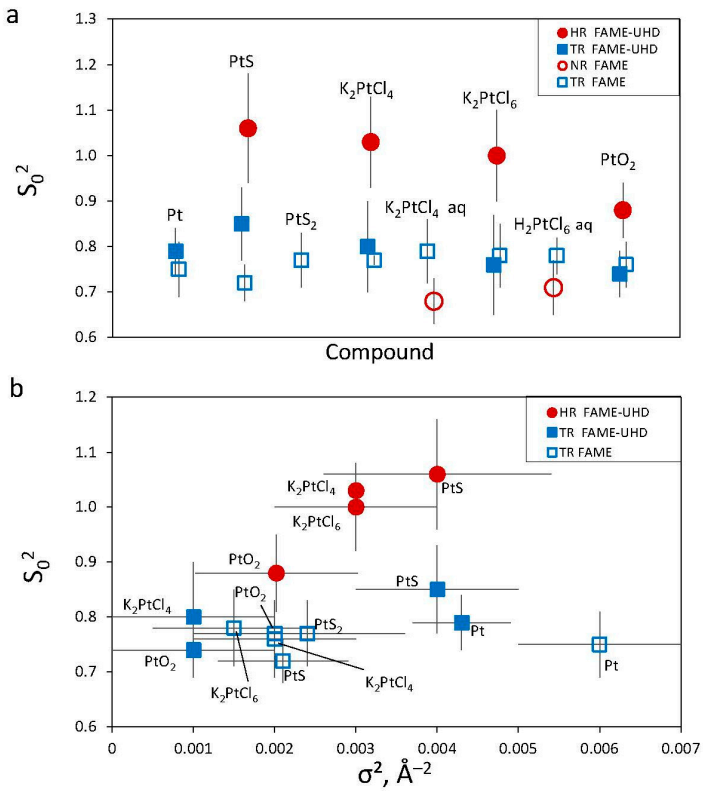

Figure 9. (**a**) Amplitude reduction factor, S_0^2, derived from EXAFS fits of the indicated reference compounds (see Table 3). (**b**) The same value of S_0^2 plotted versus σ^2 of the first coordination shell for the indicated reference compounds and acquisition modes. Mean S_0^2 values are 0.76 ± 0.04 and 0.99 ± 0.07 (1 standard error) in TR and HR mode, respectively.

4.3. Modeling Disorder Using Mean Square Relative Displacement, σ^2

To investigate the potential influence of σ^2 on the S_0^2 determination, these parameters that are strongly correlated in the EXAFS formula must be decoupled. To do so, we

performed EXAFS fits on several samples (Figure 10), whose spectra were acquired both in HR and TR modes, by fixing the σ^2 value to the mean value derived from HR and TR mode spectra for the same Pt solid compound (Table 3). The newly obtained S_0^2 values still present similar systematic differences between HR and TR modes (~0.15; Table A3, Figure 10b). In contrast, for analogous fits, performed by fixing the mean S_0^2, the obtained σ^2 values overlap within their uncertainties between HR and TR modes (Figure 10c). Thus, despite the apparent correlation between S_0^2 and σ^2 (Figures 9b and 10b), the S_0^2 values are distinctly different for a given solid between the two modes, in contrast to the largely overlapping σ^2 values. This analysis demonstrates a relatively minor effect of σ^2 compared to S_0^2 on the EXAFS fits between TR/NR and HR modes. The increase in EXAFS amplitude at low k values clearly highlights the gain of amplitude in HR-EXAFS, while the influence of σ^2 is less apparent, being partly obscured by the growing noise at higher k values. The greater amplitude is therefore compensated by a significantly greater S_0^2 value in HR-EXAFS fits.

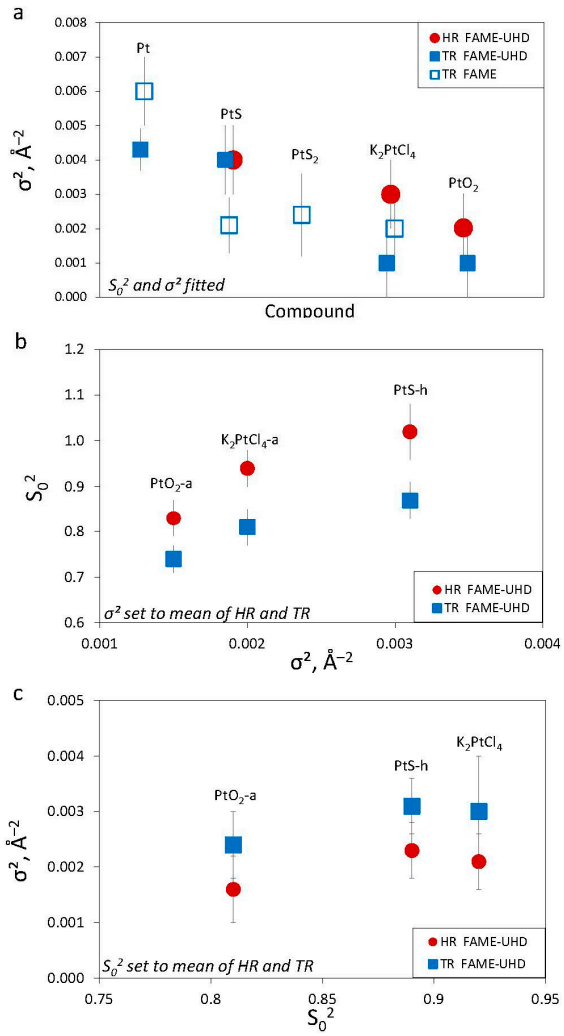

Figure 10. The values of σ^2 of the first coordination shell for the investigated solid samples with indicated acquisition modes (from Table 3) (**a**), amplitude reduction factor (S_0^2) versus the mean σ^2 value (from Table A3) (**b**), and σ^2 value versus the mean S_0^2 value (from Table A4) (**c**). The S_0^2 values are always significantly higher in HR than in TR mode, whereas the σ^2 values are similar within their uncertainties. The X-axis position of the HR points is slightly shifted in (**c**) to avoid overlap of the graph.

4.4. Implications

The systematic difference in the S_0^2 values revealed between HR and NR/TR acquisition modes highlights the necessity of the accurate determination of S_0^2 in different acquisition modes. This necessity may be particularly crucial when determining coordination numbers, as we have demonstrated using the $(NH_4)_2Pt^{IV}(S_5)_3$ sample. For example, using a "wrong" S_0^2 value (0.76) established by fitting conventional transmission spectra of Pt references, yields a significant overestimation of the first shell Pt-S coordination number, $N(S_1) = 7.4 \pm 0.5$ instead of the right value of 6, when EXAFS fits HR fluorescence spectra, while neither the R nor σ^2 value would be significantly affected. These results demonstrate the much larger influence of S_0^2 than σ^2 on the determination of coordination numbers, at least for EXAFS spectra with comparable signal-to-noise ratios at relatively low k values (<10 $Å^{-1}$, Figure 7). More generally, the necessity of the S_0^2 value correctly calibrated in the right mode may be particularly crucial when determining ligand coordination numbers in a mixture of aqueous complexes from EXAFS data, for example, in the case of Pd-O/Cl complexes [14] or Mo-O/S complexes [102]. Note that, an error of 0.2 in S_0^2 would lead to an error of 0.4 to 0.8 sulfur atoms for the average number of HS^- ligands around Pt in an aqueous solution containing $Pt(HS)_2^0$, $Pt(HS)_3^-$, and $Pt(HS)_4^{2-}$ complexes, making it difficult to identify the major solubility-controlling complex [96]. This identification is necessary for accurate predictions of metal transport by hydrothermal fluids, e.g., [18,35].

5. Concluding Remarks

In this study, we attempted to develop robust and safe protocols of laboratory synthesis of different Pt-S-bearing solid compounds ($Pt^{II}S$, $Pt^{IV}S_2$, and $(NH_4)_2PtS_5$) that may be used as XAS references for studying Pt in natural sulfide minerals, hydrothermal fluids, and technological materials. XANES and EXAFS spectra, recorded in this study on these solids and additional Pt chloride and oxide compounds, contribute to the extension of an open-access XAS reference database (SSHADE). Spectra recorded in HERFD mode present a significant gain in resolution compared to conventional fluorescence spectra, both in energy position and amplitude/width of the white-line and post-edge XANES features. This gain may be crucial when quantifying Pt^{II}/Pt^{IV} redox and Cl/S ligand ratios in samples that contain a mixture of different Pt complexes and redox states. EXAFS spectra in all modes (transmission, fluorescence, and HR-fluorescence) yield identical structural parameters in terms of interatomic distances, in good agreement with available crystallographic values. However, the amplitude reduction factor (S_0^2) derived by fitting HR fluorescence spectra, 0.99 ± 0.07, is systematically higher than the value derived from transmission and conventional fluorescence spectra, 0.76 ± 0.04. This difference is explained by the larger EXAFS amplitudes in HR-fluorescence than in transmission or NR-fluorescence, and highlights the importance of using the right acquisition mode to be able to better constrain the S_0^2 parameter and to use it for more accurate derivations of coordination numbers in unknown samples. The HR mode appears, in addition, to be particularly interesting for complex natural or industrial Pt samples containing elements with close absorption edge energies (W, Au, As, Ta, Re).

Author Contributions: Conceptualization, project administration, and writing were carried out by C.L. and G.S.P.; experimental work on FAME beamlines was performed by C.L., E.F.B., J.-L.H., E.D., M.A.K. and G.S.P.; solid syntheses were performed by C.L., M.A.K., S.F. and O.L.; interpretation of XAS data by C.L., E.F.B. and J.-L.H. All authors have read and agreed to the published version of the manuscript.

Funding: This work was funded by the French National Research Agency (grant RadicalS—ANR-16-CE31-0017), the Institut Carnot ISIFoR (grants OrPet and AsCOCrit), and the Centre National de la Recherche Scientifique through the Mission pour les initiatives transverses et interdisciplinaires (MITI) interdisciplinary programs (Grant PtS3, MétalloMix-2021). The FAME-UHD project is supported by the French Grand Emprunt EquipEx (EcoX ANR-10-EQPX-27-01), the CEA-CNRS CRG consortium,

and the INSU-CNRS institute. The HP/HT vessel was financially supported by the French "grand emprunt" EquipEx (PlanEx, ANR-11-EQPX-36).

Data Availability Statement: The XAS spectra presented in this study are openly available in the SSHADE database (https://www.sshade.eu/, accessed on 8 December 2022): 10.26302/SSHADE/EXPERIMENT_GP_20180208_001, 10.26302/SSHADE/EXPERIMENT_GP_20181107_001, 10.26302/SSHADE/EXPERIMENT_CL_20210211_001.

Acknowledgments: C.L. acknowledges support from the University of Toulouse (fellowship of the Ministère de l'Enseignement Supérieur et de la Recherche, MESR). We acknowledge the European Synchrotron Radiation Facility for providing beamtime and facilities. We would like to thank O. Proux, E. Lahera, I. Kieffer, D. Testemale, B. Schmitt, P. Gisquet, A. Castillo, T. Aigouy, F. Maube, L. Menjot, C. Routaboul, C.L. Serpentini, J. Babinot, and V. Chardès for their invaluable help with experiments and chemical and data analyses. Comments of four anonymous referees greatly improved the article.

Conflicts of Interest: The authors declare no conflict of interest.

Appendix A

Laskar et al.

Exploring Platinum Speciation with X-ray Absorption Spec-troscopy under High-Energy Resolution Fluorescence Detection mode.

This file contains: Tables A1–A4 and Figures A1–A6.

Table A1. Positions of the absorption edge (edge jump EJ; maximum of the first derivative) and the maximum of the white line (WL) of Pt L_{III}-edge XANES spectra of the Pt compounds investigated in this study in different modes (HR vs. TR and NR). Spectra were calibrated with a Pt foil. Uncertainty of the energy values is ±0.3 eV.

Sample/Standard	Feature	Position, eV This Study	Literature	WL Amplitude (Normalized Spectra) HR	TR or NR
Pt^0	EJ WL	11,564.0 11,565.5	11,564.0 [a] 11,565.5 [a]	–	1.29
$Pt^{II}S$-h	EJ WL	11,565.6 11,566.9	11,564.5 [a] 11,567.5 [a]	2.66	1.35
$(NH_4)_2Pt^{IV}(S_5)_3$	EJ WL	11,566.7 11,567.8	– –	3.55	1.71
$K_2Pt^{II}Cl_4$-a	EJ WL	11,565.0 11,566.1	11,563.5 [b] 11,566.0 [b]	3.35	1.48
$K_2Pt^{IV}Cl_6$-a	EJ WL	11,567.2 11,568.0	11,565.5 [b] 11,567.7 [b]	5.62	2.24
$Pt^{IV}O_2$-a	EJ WL	11,567.5 11,568.4	11,565.6 [c] 11,567.8 [c]	5.88	2.49
$C_6H_{12}N_2O_4Pt^{II}$	EJ WL	11,566.2 11,567.5	– –	3.20	1.65

High-resolution mode (HR), and conventional mode analogues (transmission, TR, and nominal-resolution total fluorescence yield, TFY—NR). [a] Ref. [28], calibrated with a Pt foil (EJ: 11,564.0 eV and WL: 11,566.5 eV). [b] Ref. [16], calibrated with a Pt foil (EJ: 11,564 eV). [c] Ref. [30], calibrated with a Pt foil (EJ: 11,564 eV).

Table A2. Ratio between the maximum amplitude absorption at the white line (WL) of the normalized XANES spectra for the indicated pairs of compounds. Note that ratios in HR-fluorescence mode are always higher than in transmission mode (TR), demonstrating an improved spectral contrast in HR mode.

	Pt^{IV}-Cl/Pt^{II}-Cl	Pt^{IV}-S/Pt^{II}-S	Pt^{II}-Cl/Pt^{II}-S	Pt^{IV}-Cl/Pt^{IV}-S
HR-XANES	1.68	1.34	1.26	1.58
TR-XANES	1.52	1.28	1.10	1.31

Pt^{IV}-Cl = $K_2Pt^{IV}Cl_6$-a; Pt^{II}-Cl = $K_2Pt^{II}Cl_4$-a; Pt^{IV}-S = $(NH_4)_2Pt^{IV}(S_5)_3$; Pt^{II}-S = $Pt^{II}S$-h.

Table A3. Parameters of the Pt local atomic structure in the Pt solids obtained by fitting Pt L_{III}-edge EXAFS spectra, by setting the σ^2 value to the mean value between those obtained in HR-fluorescence (HR) and transmission (TR) modes from Table 3.

Compound	$\sigma^2 \times 10^3$, $Å^{-2}$	Mode	$S_0{}^2$	Δe, eV	Pt-X [a], Å	*R*-Factor × 10^3
K_2PtCl_4-a	2.0	TR	0.82 (4)	9 (1)	2.293 (7)	43
K_2PtCl_4-a	2.0	HR	0.94 (4)	7 (1)	2.300 (6)	23
PtS-h	3.1	TR	0.87 (4)	10 (1)	2.303 (6)	39
PtS-h	3.1	HR	1.02 (6)	6 (1)	2.301 (7)	34
PtO_2-a	1.5	TR	0.74 (3)	12 (1)	2.009 (6)	33
PtO_2-a	1.5	HR	0.83 (4)	9 (1)	2.018 (6)	28

[a] X = Cl or S or O in the 1st shell.

Table A4. Parameters of the Pt local atomic structure in the Pt solids obtained by fitting Pt L_{III}-edge EXAFS spectra, by setting the $S_0{}^2$ value to the mean value between those in HR-fluorescence (HR) and transmission (TR) modes from Table 3.

Compound	$S_0{}^2$	Mode	$\sigma^2 \times 10^3$, $Å^{-2}$	Δe, eV	Pt-X [a], Å	*R*-Factor × 10^3
K_2PtCl_4-a	0.92	TR	3 (1)	9 (1)	2.292 (8)	49
K_2PtCl_4-a	0.92	HR	2.1 (5)	7 (1)	2.300 (7)	22
PtS-h	0.89	TR	3.1 (5)	10 (1)	2.303 (6)	30
PtS-h	0.89	HR	2.3 (5)	6 (1)	2.300 (8)	39
PtO_2-a	0.81	TR	2.4 (6)	12 (1)	2.010 (7)	36
PtO_2-a	0.81	HR	1.6 (6)	9 (1)	2.019 (6)	27

[a] X = Cl or S or O in the 1st shell.

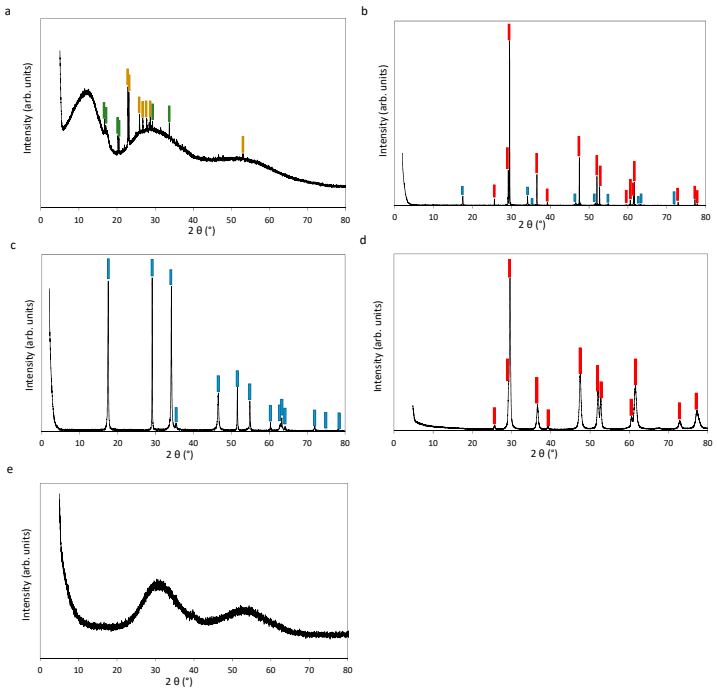

Figure A1. Diffraction patterns (in black color) of the synthesized $(NH_4)_2Pt^{IV}(S_5)_3$ (**a**), $Pt^{II}S$-s (**b**), $Pt^{IV}S_2$-s (**c**), $Pt^{II}S$-h (**d**), and $Pt^{IV}S_2$-c (**e**). PtS and PtS_2 reference peaks are in red, and in blue, respectively. For (**a**,**e**), the spectral shape shows an amorphous pattern, with for (**a**) the presence of residual $(NH_4)_2SO_4$ and S shown in green and yellow, respectively. For (**b**–**d**), the solid is highly crystalline. For (**a**), the first "hill" observed (2θ~13°) is close to the main XRD peak of crystalline $(NH_4)_2Pt^{IV}(S_5)_3$ (4 intense peaks at 11.3°, 12.4°, 12.7°, and 13.7°; [90]), but the 2 other "hills" at higher angles are more difficult to constrain because they are wider and less intense and XRD peaks reported for the crystalline compound are too numerous and too weak. For (**e**), the two "hills" (at ~30° and ~55°) are those of amorphous sulfur. In sample (**b**), small amount of PtS_2 was obtained in the synthesis in addition to PtS.

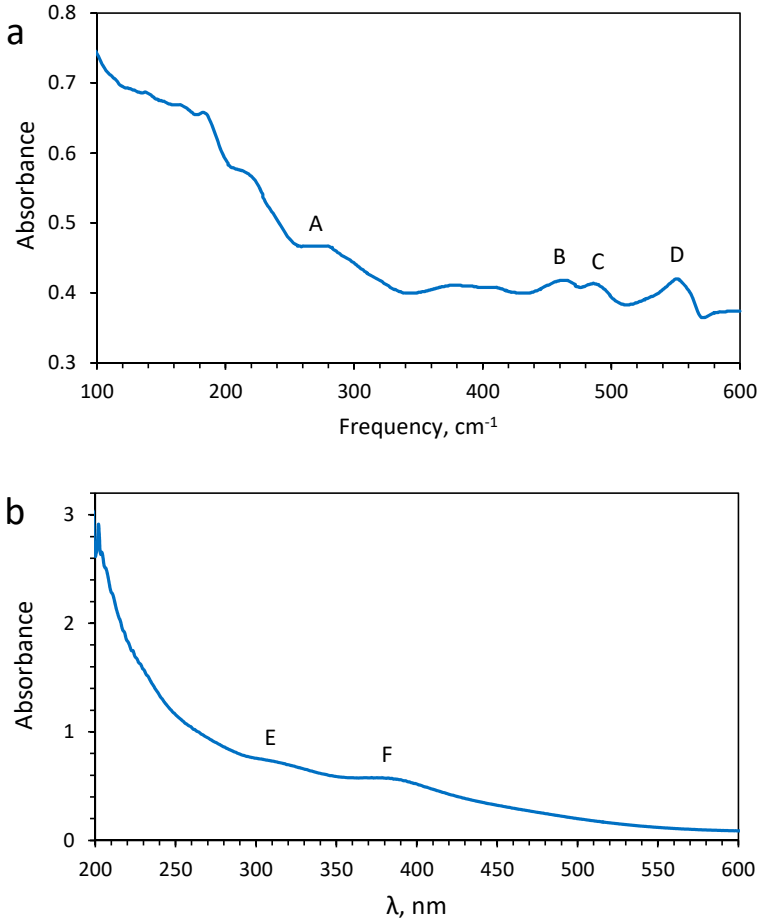

Figure A2. (**a**) Far-infrared spectrum and (**b**) UV-visible spectrum of synthesized $(NH_4)_2Pt^{IV}(S_5)_3$. The main absorbance peaks in (**a**) are at 278 cm^{-1} (A), 461 cm^{-1} (B), 487 cm^{-1} (C), 551 cm^{-1} (D). The two main absorbance peaks above the cutoff of 200 nm in (**b**) are at 290 nm (E) and 385 nm (F).

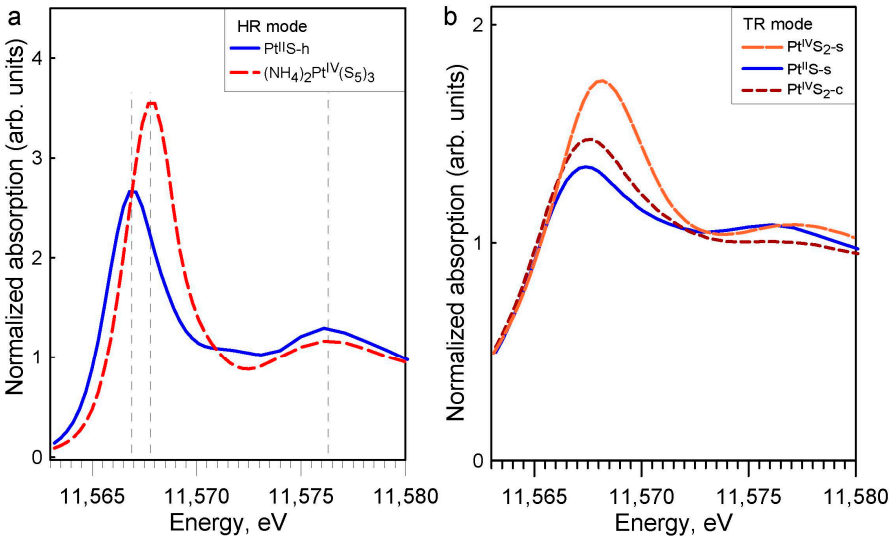

Figure A3. (**a**) Normalized Pt L_{III}-edge XANES spectra in HR mode for the two Pt-S solid compounds, $Pt^{II}S$-h and $(NH_4)_2Pt^{IV}(S_5)_3$. (**b**) Normalized Pt L_{III}-edge XANES spectra in TR mode for synthesized $Pt^{II}S$-s, $Pt^{IV}S_2$-s, and $Pt^{IV}S_2$-c. The commercial $Pt^{IV}S_2$-c solid is impure, containing mostly PtS and S with a little amount of PtS_2.

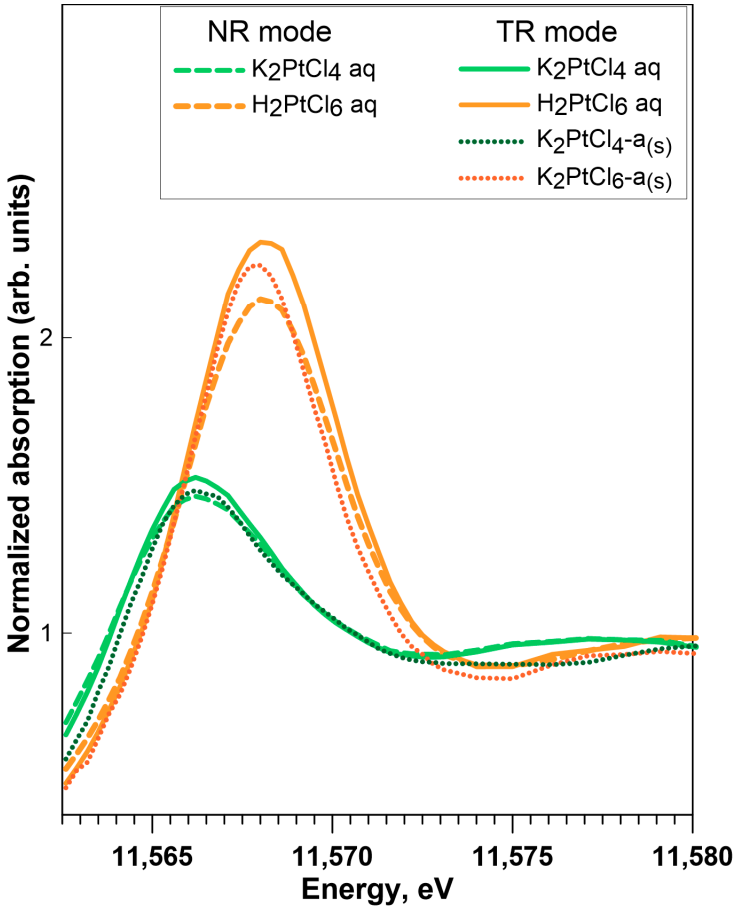

Figure A4. Normalized Pt L_{III}-edge XANES spectra in nominal-resolution fluorescence (NR) and transmission (TR) modes for aqueous samples $K_2PtCl_{4(aq)}$ and $H_2PtCl_{6(aq)}$, compared with their respective solid counterparts $K_2PtCl_{4(s)}$ and $K_2PtCl_{6(s)}$ in TR mode. Both modes give similar shapes and amplitudes of the white line.

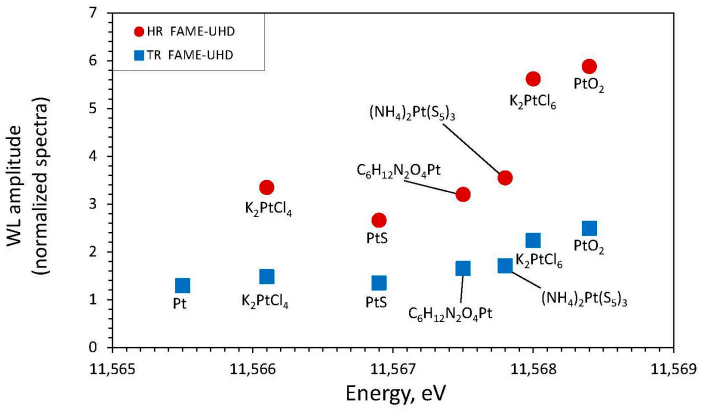

Figure A5. White-line amplitudes of normalized Pt L_{III}-edge XANES spectra in high-resolution fluorescence (HR) and transmission (TR) modes for aqueous solid samples. Amplitudes are always significantly higher in HR than in TR modes. Data are from Table A1.

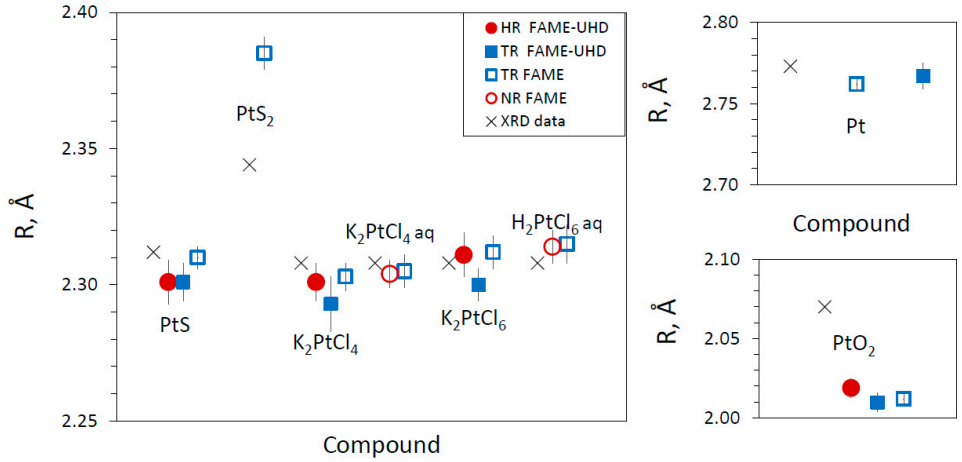

Figure A6. Distances Pt-X (X = Pt, S, Cl or O) determined from EXAFS modeling compared with XRD values. Data are from Table 3.

References

1. Jha, M.K.; Lee, J.; Kim, M.; Jeong, J.; Kim, B.-S.; Kumar, V. Hydrometallurgical Recovery/Recycling of Platinum by the Leaching of Spent Catalysts: A Review. *Hydrometallurgy* **2013**, *133*, 23–32. [CrossRef]
2. Kawde, A.-N.; Aziz, M.; Baig, N.; Temerk, Y. A Facile Fabrication of Platinum Nanoparticle-Modified Graphite Pencil Electrode for Highly Sensitive Detection of Hydrogen Peroxide. *J. Electroanal. Chem.* **2015**, *740*, 68–74. [CrossRef]
3. Bingwa, N.; Ndolomingo, M.J.; Noh, J.-H.; Antonels, N.; Carleschi, E.; Doyle, B.P.; Haumann, M.; Meijboom, R. Synergistic Effect of Mesoporous Metal Oxides and PtO_2 Nanoparticles in Aerobic Oxidation of Ethanol and Ionic Liquid Induced Acetaldehyde Selectivity. *Mol. Catal.* **2020**, *492*, 110978. [CrossRef]
4. Loibl, S.; O'Shaughnessy, J.; Untch, M.; Sikov, W.M.; Rugo, H.S.; McKee, M.D.; Huober, J.; Golshan, M.; von Minckwitz, G.; Maag, D.; et al. Addition of the PARP Inhibitor Veliparib plus Carboplatin or Carboplatin Alone to Standard Neoadjuvant Chemotherapy in Triple-Negative Breast Cancer (BrighTNess): A Randomised, Phase 3 Trial. *Lancet Oncol.* **2018**, *19*, 497–509. [CrossRef]
5. Ghosh, S. Cisplatin: The First Metal Based Anticancer Drug. *Bioorg. Chem.* **2019**, *88*, 102925. [CrossRef]
6. Tutt, A.; Tovey, H.; Cheang, M.C.U.; Kernaghan, S.; Kilburn, L.; Gazinska, P.; Owen, J.; Abraham, J.; Barrett, S.; Barrett-Lee, P.; et al. A Randomised Phase III Trial of Carboplatin Compared with Docetaxel in BRCA1/2 Mutated and Pre-Specified Triple Negative Breast Cancer "BRCAness" Subgroups: The TNT Trial. *Nat. Med.* **2019**, *24*, 628. [CrossRef]
7. Cotton, F.A.; Wilkinson, G.; Murillo, C.A.; Bochmann, M. *Advanced Inorganic Chemistry*, 6th ed.; Wiley: New York, NY, USA, 1999.
8. Chen, K.; Walker, R.J.; Rudnick, R.L.; Gao, S.; Gaschnig, R.M.; Puchtel, I.S.; Tang, M.; Hu, Z.-C. Platinum-Group Element Abundances and Re–Os Isotopic Systematics of the Upper Continental Crust through Time: Evidence from Glacial Diamictites. *Geochim. Cosmochim. Acta* **2016**, *191*, 1–16. [CrossRef]
9. Ballhaus, C.G.; Stumpfl, E.F. Sulfide and Platinum Mineralization in the Merensky Reef: Evidence from Hydrous Silicates and Fluid Inclusions. *Contrib. Miner. Pet.* **1986**, *94*, 193–204. [CrossRef]
10. Gammons, C.H.; Bloom, M.S. Experimental Investigation of the Hydrothermal Geochemistry of Platinum and Palladium: II. The Solubility of PtS and PdS in Aqueous Sulfide Solutions to 300 °C. *Geochim. Cosmochim. Acta* **1993**, *57*, 2451–2467. [CrossRef]
11. Pan, P.; Wood, S.A. Solubility of Pt and Pd Sulfides and Au Metal in Aqueous Bisulfide Solutions: II. Results at 200° to 350 °C and Saturated Vapor Pressure. *Miner. Depos.* **1994**, *29*, 373–390. [CrossRef]
12. Sassani, D.C.; Shock, E.L. Solubility and Transport of Platinum-Group Elements in Supercritical Fluids: Summary and Estimates of Thermodynamic Properties for Ruthenium, Rhodium, Palladium, and Platinum Solids, Aqueous Ions, and Complexes to 1000 °C and 5 Kbar. *Geochim. Cosmochim. Acta* **1998**, *62*, 2643–2671. [CrossRef]
13. Fleet, M.E.; Liu, X. X-ray Absorption Spectroscopy of Ultramarine Pigments: A New Analytical Method for the Polysulfide Radical Anion S_3^- Chromophore. *Spectrochim. Acta Part B At. Spectrosc.* **2010**, *65*, 75–79. [CrossRef]
14. Bazarkina, E.F.; Pokrovski, G.S.; Hazemann, J.-L. Structure, Stability and Geochemical Role of Palladium Chloride Complexes in Hydrothermal Fluids. *Geochim. Cosmochim. Acta* **2014**, *146*, 107–131. [CrossRef]
15. Kokh, M.A.; Akinfiev, N.N.; Pokrovski, G.S.; Salvi, S.; Guillaume, D. The Role of Carbon Dioxide in the Transport and Fractionation of Metals by Geological Fluids. *Geochim. Cosmochim. Acta* **2017**, *197*, 433–466. [CrossRef]
16. Tagirov, B.R.; Filimonova, O.N.; Trigub, A.L.; Akinfiev, N.N.; Nickolsky, M.S.; Kvashnina, K.O.; Chareev, D.A.; Zotov, A.V. Platinum Transport in Chloride-Bearing Fluids and Melts: Insights from in Situ X-ray Absorption Spectroscopy and Thermodynamic Modeling. *Geochim. Cosmochim. Acta* **2019**, *254*, 86–101. [CrossRef]
17. Filimonova, O.N.; Tagirov, B.R.; Zotov, A.V.; Baranova, N.N.; Bychkova, Y.V.; Tyurin, D.A.; Chareev, D.A.; Nickolsky, M.S. The Solubility of Cooperite PtS(Cr) at 25–450 °C, P_{sat}—1000 Bar and Hydrosulfide Complexing of Platinum in Hydrothermal Fluids. *Chem. Geol.* **2021**, *559*, 119968. [CrossRef]

18. Pokrovski, G.S.; Kokh, M.A.; Desmaele, E.; Laskar, C.; Bazarkina, E.F.; Borisova, A.Y.; Testemale, D.; Hazemann, J.-L.; Vuilleumier, R.; Ferlat, G.; et al. The Trisulfur Radical Ion $S_3^{\bullet-}$ Controls Platinum Transport by Hydrothermal Fluids. *Proc. Natl. Acad. Sci. USA* **2021**, *118*, e2109768118. [CrossRef]
19. Huang, H.; Liang, C.H.; Penner-Hahn, J.E. X-ray Absorption Spectroscopy of Dimethylcuprates: Evidence for Solvent-Dependent Aggregation. *Angew. Chem. Int. Ed.* **1998**, *37*, 1564–1566. [CrossRef]
20. Ho, P.K.-H.; Chua, L.-L.; Dipankar, M.; Gao, X.Y.; Qi, D.C.; Wee, A.T.-S.; Chang, J.-F.; Friend, R.H. Solvent Effects on Chain Orientation and Interchain π-Interaction in Conjugated Polymer Thin Films: Direct Measurements of the Air and Substrate Interfaces by Near-Edge X-ray Absorption Spectroscopy. *Adv. Mater.* **2007**, *19*, 215–221. [CrossRef]
21. Bokarev, S.I.; Dantz, M.; Suljoti, E.; Kühn, O.; Aziz, E.F. State-Dependent Electron Delocalization Dynamics at the Solute-Solvent Interface: Soft-X-ray Absorption Spectroscopy and Ab Initio Calculations. *Phys. Rev. Lett.* **2013**, *111*, 083002. [CrossRef]
22. Penfold, T.J.; Karlsson, S.; Capano, G.; Lima, F.A.; Rittmann, J.; Reinhard, M.; Rittmann-Frank, M.H.; Braem, O.; Baranoff, E.; Abela, R.; et al. Solvent-Induced Luminescence Quenching: Static and Time-Resolved X-ray Absorption Spectroscopy of a Copper(I) Phenanthroline Complex. *J. Phys. Chem. A* **2013**, *117*, 4591–4601. [CrossRef]
23. Asakura, H.; Tanaka, T. Recent Applications of X-ray Absorption Spectroscopy in Combination with High Energy Resolution Fluorescence Detection. *Chem. Lett.* **2021**, *50*, 1075–1085. [CrossRef]
24. Peyrelade, E. Élaborations et Caractérisations Electrochimiques et Physiques de Matériaux D'anode de PEMFC peu Sensibles à L'empoisonnement par CO: Étude D'alliages et de Composites à Base de Platine-Molybdène et de Platine-Tungstène. Ph.D. Thesis, Institut National Polytechnique de Grenoble, Grenoble, France, 2005.
25. Crowther, N. Catalyseurs à Base de Complexes de Platine Incorporés Dans Les Murs de Silices Mesoporeuses Périodiques; Réactivité En Hydrogénation. Ph.D. Thesis, Ecole Normale Supérieure de Lyon-ENS LYON, Lyon, France, 2007.
26. Gorczyca, A.; Moizan, V.; Chizallet, C.; Proux, O.; Del Net, W.; Lahera, E.; Hazemann, J.-L.; Raybaud, P.; Joly, Y. Monitoring Morphology and Hydrogen Coverage of Nanometric Pt/γ-Al_2O_3 Particles by In Situ HERFD-XANES and Quantum Simulations. *Angew. Chem.* **2014**, *126*, 12634–12637. [CrossRef]
27. Scholten, L.; Watenphul, A.; Beermann, O.; Testemale, D.; Ames, D.; Schmidt, C. Nickel and Platinum in High-Temperature H_2O + HCl Fluids: Implications for Hydrothermal Mobilization. *Geochim. Cosmochim. Acta* **2018**, *224*, 187–199. [CrossRef]
28. Filimonova, O.N.; Nickolsky, M.S.; Trigub, A.L.; Chareev, D.A.; Kvashnina, K.O.; Kovalchuk, E.V.; Vikentyev, I.V.; Tagirov, B.R. The State of Platinum in Pyrite Studied by X-ray Absorption Spectroscopy of Synthetic Crystals. *Econ. Geol.* **2019**, *114*, 1649–1663. [CrossRef]
29. Filimonova, O.N.; Trigub, A.L.; Nickolsky, M.S.; Chareev, D.A.; Kvashnina, K.O.; Kovalchuk, E.V.; Vikentyev, I.V.; Reukov, V.L.; Tagirov, B.R. The State of Platinum in Pyrrhotite: X-ray Absorption Spectroscopy Study and Implications for the Role of Fe Sulphides as Platinum Carriers. *Mineral. Mag.* **2021**, *85*, 846–861. [CrossRef]
30. Evstigneeva, P.V.; Trigub, A.L.; Chareev, D.A.; Nickolsky, M.S.; Tagirov, B.R. The Charge State of Pt in Binary Compounds and Synthetic Minerals Determined by X-ray Absorption Spectroscopy and Quantum Chemical Calculations. *Minerals* **2021**, *11*, 79. [CrossRef]
31. Hämäläinen, K.; Siddons, D.P.; Hastings, J.B.; Berman, L.E. Elimination of the Inner-Shell Lifetime Broadening in X-ray-Absorption Spectroscopy. *Phys. Rev. Lett.* **1991**, *67*, 2850. [CrossRef]
32. Galoisy, L.; Calas, G.; Arrio, M.A. High-Resolution XANES Spectra of Iron in Minerals and Glasses: Structural Information from the Pre-Edge Region. *Chem. Geol.* **2001**, *174*, 307–319. [CrossRef]
33. Glatzel, P.; Sikora, M.; Smolentsev, G.; Fernández-García, M. Hard X-ray Photon-in Photon-out Spectroscopy. *Catal. Today* **2009**, *145*, 294–299. [CrossRef]
34. Isaure, M.-P.; Albertelli, M.; Kieffer, I.; Tucoulou, R.; Petrel, M.; Gontier, E.; Tessier, E.; Monperrus, M.; Goñi-Urriza, M. Relationship Between Hg Speciation and Hg Methylation/Demethylation Processes in the Sulfate-Reducing Bacterium Pseudodesulfovibrio Hydrargyri: Evidences From HERFD-XANES and Nano-XRF. *Front. Microbiol.* **2020**, *11*, 584715. [CrossRef] [PubMed]
35. Thomas, S.A.; Mishra, B.; Myneni, S.C.B. Cellular Mercury Coordination Environment, and Not Cell Surface Ligands, Influence Bacterial Methylmercury Production. *Environ. Sci. Technol.* **2020**, *54*, 3960–3968. [CrossRef]
36. Pokrovski, G.S.; Escoda, C.; Blanchard, M.; Testemale, D.; Hazemann, J.-L.; Gouy, S.; Kokh, M.A.; Boiron, M.-C.; de Parseval, F.; Aigouy, T.; et al. An Arsenic-Driven Pump for Invisible Gold in Hydrothermal Systems. *Geochem. Perspect. Lett.* **2021**, *17*, 39–44. [CrossRef]
37. Pokrovski, G.S.; Desmaele, E.; Laskar, C.; Bazarkina, E.F.; Testemale, D.; Hazemann, J.-L.; Vuilleumier, R.; Seitsonen, A.P.; Ferlat, G.; Saitta, A.M. Gold Speciation in Hydrothermal Fluids Revealed by in Situ High Energy Resolution X-ray Absorption Spectroscopy. *Am. Miner. J. Earth Planet. Mater.* **2022**, *107*, 369–376. [CrossRef]
38. Proux, O.; Lahera, E.; Del Net, W.; Kieffer, I.; Rovezzi, M.; Testemale, D.; Irar, M.; Thomas, S.; Aguilar-Tapia, A.; Bazarkina, E.F.; et al. High-Energy Resolution Fluorescence Detected X-ray Absorption Spectroscopy: A Powerful New Structural Tool in Environmental Biogeochemistry Sciences. *J. Environ. Qual.* **2017**, *46*, 1146–1157. [CrossRef] [PubMed]
39. De Groot, F.M.F.; Krisch, M.H.; Vogel, J. Spectral Sharpening of the Pt L Edges by High-Resolution x-Ray Emission. *Phys. Rev. B* **2002**, *66*, 195112. [CrossRef]
40. Singh, J.; Tromp, M.; Safonova, O.V.; Glatzel, P.; van Bokhoven, J.A. In Situ XAS with High-Energy Resolution: The Changing Structure of Platinum during the Oxidation of Carbon Monoxide. *Catal. Today* **2009**, *145*, 300–306. [CrossRef]

41. Iglesias-Juez, A.; Beale, A.M.; Maaijen, K.; Weng, T.C.; Glatzel, P.; Weckhuysen, B.M. A Combined in Situ Time-Resolved UV–Vis, Raman and High-Energy Resolution X-ray Absorption Spectroscopy Study on the Deactivation Behavior of Pt and PtSn Propane Dehydrogenation Catalysts under Industrial Reaction Conditions. *J. Catal.* **2010**, *276*, 268–279. [CrossRef]
42. Friebel, D.; Miller, D.J.; Nordlund, D.; Ogasawara, H.; Nilsson, A. Degradation of Bimetallic Model Electrocatalysts: An In Situ X-ray Absorption Spectroscopy Study. *Angew. Chem. Int. Ed.* **2011**, *50*, 10190–10192. [CrossRef]
43. Friebel, D.; Miller, D.J.; O'Grady, C.P.; Anniyev, T.; Bargar, J.; Bergmann, U.; Ogasawara, H.; Wikfeldt, K.T.; Pettersson, L.G.; Nilsson, A. In Situ X-ray Probing Reveals Fingerprints of Surface Platinum Oxide. *Phys. Chem. Chem. Phys.* **2011**, *13*, 262–266. [CrossRef]
44. Merte, L.R.; Behafarid, F.; Miller, D.J.; Friebel, D.; Cho, S.; Mbuga, F.; Sokaras, D.; Alonso-Mori, R.; Weng, T.-C.; Nordlund, D. Electrochemical Oxidation of Size-Selected Pt Nanoparticles Studied Using in Situ High-Energy-Resolution X-ray Absorption Spectroscopy. *ACS Catal.* **2012**, *2*, 2371–2376. [CrossRef]
45. Qureshi, M.; Garcia-Esparza, A.T.; Jeantelot, G.; Ould-Chikh, S.; Aguilar-Tapia, A.; Hazemann, J.-L.; Basset, J.-M.; Loffreda, D.; Le Bahers, T.; Takanabe, K. Catalytic Consequences of Ultrafine Pt Clusters Supported on $SrTiO_3$ for Photocatalytic Overall Water Splitting. *J. Catal.* **2019**, *376*, 180–190. [CrossRef]
46. Batista, A.T.F.; Baaziz, W.; Taleb, A.-L.; Chaniot, J.; Moreaud, M.; Legens, C.; Aguilar-Tapia, A.; Proux, O.; Hazemann, J.-L.; Diehl, F.; et al. Atomic Scale Insight into the Formation, Size, and Location of Platinum Nanoparticles Supported on γ-Alumina. *ACS Catal.* **2020**, *10*, 4193–4204. [CrossRef]
47. Maurer, F.; Jelic, J.; Wang, J.; Gänzler, A.; Dolcet, P.; Wöll, C.; Wang, Y.; Studt, F.; Casapu, M.; Grunwaldt, J.-D. Tracking the Formation, Fate and Consequence for Catalytic Activity of Pt Single Sites on CeO_2. *Nat. Catal.* **2020**, *3*, 824–833. [CrossRef]
48. Piccolo, L.; Afanasiev, P.; Morfin, F.; Len, T.; Dessal, C.; Rousset, J.L.; Aouine, M.; Bourgain, F.; Aguilar-Tapia, A.; Proux, O.; et al. *Operando* X-ray Absorption Spectroscopy Investigation of Photocatalytic Hydrogen Evolution over Ultradispersed Pt/TiO_2 Catalysts. *ACS Catal.* **2020**, *10*, 12696–12705. [CrossRef]
49. Chen, J.; Finfrock, Y.Z.; Wang, Z.; Sham, T.-K. High Energy Resolution Fluorescence Detection of the Pt $L_{3,2}$-Edge Whitelines of Pt-Based Bimetallic Systems: Implications for the Pt $5d_{5/2,3/2}$ Density of States. *J. Phys. Chem. C* **2021**, *125*, 2327–2333. [CrossRef]
50. Srinath, N.V.; Poelman, H.; Buelens, L.; Dendooven, J.; Reyniers, M.-F.; Marin, G.B.; Galvita, V.V. Behaviour of Platinum-Tin during CO_2-Assisted Propane Dehydrogenation: Insights from Quick X-ray Absorption Spectroscopy. *J. Catal.* **2022**, *408*, 356–371. [CrossRef]
51. Laskar, C. Impact Du Soufre Sur Le Transport Des Platinoïdes Par Les Fluides Hydrothermaux. Ph.D. Thesis, University of Toulouse III, Toulouse, France, 2022.
52. Pokrovski, G.S.; Tagirov, B.R.; Schott, J.; Hazemann, J.-L.; Proux, O. A New View on Gold Speciation in Sulfur-Bearing Hydrothermal Fluids from in Situ X-ray Absorption Spectroscopy and Quantum-Chemical Modeling. *Geochim. Cosmochim. Acta* **2009**, *73*, 5406–5427. [CrossRef]
53. Mei, Y.; Sherman, D.M.; Liu, W.; Brugger, J. Complexation of Gold in S_3^--Rich Hydrothermal Fluids: Evidence from Ab-Initio Molecular Dynamics Simulations. *Chem. Geol.* **2013**, *347*, 34–42. [CrossRef]
54. Pokrovski, G.S.; Dubessy, J. Stability and Abundance of the Trisulfur Radical Ion S_3^- in Hydrothermal Fluids. *Earth Planet. Sci. Lett.* **2015**, *411*, 298–309. [CrossRef]
55. Cawthorn, R.G. Stratiform Platinum-Group Element Deposits in Layered Intrusions. In *Exploration for Platinum-Group Element Deposits*; Mungall, J.E., Ed.; Mineralogical Association of Canada: Québec City, QC, Canada, 2005; pp. 57–73.
56. Godel, B.; Barnes, S.-J.; Maier, W.D. Platinum-Group Elements in Sulphide Minerals, Platinum-Group Minerals, and Whole-Rocks of the Merensky Reef (Bushveld Complex, South Africa): Implications for the Formation of the Reef. *J. Petrol.* **2007**, *48*, 1569–1604. [CrossRef]
57. Barnes, S.J.; Cruden, A.R.; Arndt, N.; Saumur, B.M. The Mineral System Approach Applied to Magmatic Ni–Cu–PGE Sulphide Deposits. *Ore Geol. Rev.* **2016**, *76*, 296–316. [CrossRef]
58. Holwell, D.A.; Adeyemi, Z.; Ward, L.A.; Smith, D.J.; Graham, S.D.; McDonald, I.; Smith, J.W. Low Temperature Alteration of Magmatic Ni-Cu-PGE Sulfides as a Source for Hydrothermal Ni and PGE Ores: A Quantitative Approach Using Automated Mineralogy. *Ore Geol. Rev.* **2017**, *91*, 718–740. [CrossRef]
59. Schmitt, B.; Bollard, P.; Damien, A.; Garenne, A.; Bonal, L.; Gorbacheva, M. The SSHADE Partner's Consortium. SSHADE: Solid Spectroscopy Hosting Architecture of Databases and Expertise and Its Databases. *Eur. Planet. Sci. Congr.* **2018**, *10*. [CrossRef]
60. Collins, R.; Kaner, R.; Russo, P.; Wold, A.; Avignant, D. High-Pressure Phase Transformation of Platinum Sulfide. *Inorg. Chem.* **1979**, *18*, 727–729. [CrossRef]
61. Dembowski, J.; Marosi, L.; Essig, M. Platinum Disulfide by XPS. *Surf. Sci. Spectra* **1993**, *2*, 133–137. [CrossRef]
62. Passaretti, J.D.; Kaner, R.B.; Kershaw, R.; Wold, A. Synthesis of Poorly Crystallized Platinum Metal Dichalcogenides. *Inorg. Chem.* **1981**, *20*, 501–503. [CrossRef]
63. Rau, H.; Kutty, T.R.N.; Guedes de Carvalho, J.R.F. High Temperature Saturated Vapour Pressure of Sulphur and the Estimation of Its Critical Quantities. *J. Chem. Thermodyn.* **1973**, *5*, 291–302. [CrossRef]
64. Zhang, L.; Ren, Y.; Liu, X.; Han, F.; Evans-Lutterodt, K.; Wang, H.; He, Y.; Wang, J.; Zhao, Y.; Yang, W. Chain Breakage in the Supercooled Liquid—Liquid Transition and Re-Entry of the λ-Transition in Sulfur. *Sci. Rep.* **2018**, *8*, 4558. [CrossRef]
65. Wickenden, A.E.; Krause, R.A. Polysulfide Chelates. II. Desulfuration of PtS_{15}^{2-} and the Synthesis of PtS_{10}^{2-}. *Inorg. Chem.* **1969**, *8*, 779–783. [CrossRef]

66. Schmidt, M.; Hoffmann, G.G. Zum nukleophilen Abbau von Tris(pentasulfido)platinat(IV), $[Pt(S_5)_3]^{2-}$, und Bis(pentasulfido) platinat(II),$[Pt(S_5)_2]^{2-}$. *Z. Für Anorg. Allg. Chem.* **1979**, *452*, 112–122. [CrossRef]
67. Rybak, W.K.; Cymbaluk, A.; Siczek, M.; Skonieczny, J. Crystallization-Induced Asymmetric Synthesis of Nonracemic Platinum(IV) Polysulfide Tris(Chelate) Complexes. *Eur. J. Inorg. Chem.* **2012**, *2012*, 3675–3679. [CrossRef]
68. Jeong, H.; Yoon, S.; Kim, J.H.; Kwak, D.-H.; Gu, D.H.; Heo, S.H.; Kim, H.; Park, S.; Ban, H.W.; Park, J.; et al. Transition Metal-Based Thiometallates as Surface Ligands for Functionalization of All-Inorganic Nanocrystals. *Chem. Mater.* **2017**, *29*, 10510–10517. [CrossRef]
69. Steudel, R.; Chivers, T. The Role of Polysulfide Dianions and Radical Anions in the Chemical, Physical and Biological Sciences, Including Sulfur-Based Batteries. *Chem. Soc. Rev.* **2019**, *48*, 3279–3319. [CrossRef]
70. Jeong, H. Synthesis of Transition Metal-Based Thiometallates for Surface Functionalization of All-Inorganic Nanocrystals. Master's Thesis, Ulsan National Institute of Science and Technology, Ulsan, Republic of Korea, 2018.
71. Proux, O.; Biquard, X.; Lahera, E.; Menthonnex, J.J.; Prat, A.; Ulrich, O.; Soldo, Y.; Trvisson, P.; Kapoujyan, G.; Perroux, G.; et al. FAME A New Beamline for XRay Absorption Investigations of VeryDiluted Systems of Environmental, Material and Biological Interests. *Phys. Scr.* **2005**, *2005*, 970. [CrossRef]
72. Hazemann, J.-L.; Proux, O.; Nassif, V.; Palancher, H.; Lahera, E.; Da Silva, C.; Braillard, A.; Testemale, D.; Diot, M.-A.; Alliot, I.; et al. High-Resolution Spectroscopy on an X-ray Absorption Beamline. *J. Synchrotron Radiat.* **2009**, *16*, 283–292. [CrossRef]
73. Llorens, I.; Lahera, E.; Delnet, W.; Proux, O.; Braillard, A.; Hazemann, J.-L.; Prat, A.; Testemale, D.; Dermigny, Q.; Gelebart, F.; et al. High Energy Resolution Five-Crystal Spectrometer for High Quality Fluorescence and Absorption Measurements on an x-Ray Absorption Spectroscopy Beamline. *Rev. Sci. Instrum.* **2012**, *83*, 063104. [CrossRef]
74. Testemale, D.; Argoud, R.; Geaymond, O.; Hazemann, J.-L. High Pressure/High Temperature Cell for X-ray Absorption and Scattering Techniques. *Rev. Sci. Instrum.* **2005**, *76*, 043905. [CrossRef]
75. Pokrovski, G.S.; Borisova, A.Y.; Roux, J.; Hazemann, J.-L.; Petdang, A.; Tella, M.; Testemale, D. Antimony Speciation in Saline Hydrothermal Fluids: A Combined X-ray Absorption Fine Structure Spectroscopy and Solubility Study. *Geochim. Cosmochim. Acta* **2006**, *70*, 4196–4214. [CrossRef]
76. Ravel, B.; Newville, M. *ATHENA*, *ARTEMIS*, *HEPHAESTUS*: Data Analysis for X-ray Absorption Spectroscopy Using *IFEFFIT*. *J. Synchrotron Radiat.* **2005**, *12*, 537–541. [CrossRef]
77. Newville, M. IFEFFIT: Interactive XAFS Analysis and FEFF Fitting. *J. Synchrotron Radiat.* **2001**, *8*, 322–324. [CrossRef]
78. Pokrovski, G.S.; Roux, J.; Hazemann, J.-L.; Testemale, D. An X-ray Absorption Spectroscopy Study of Argutite Solubility and Aqueous Ge(IV) Speciation in Hydrothermal Fluids to 500 °C and 400 Bar. *Chem. Geol.* **2005**, *217*, 127–145. [CrossRef]
79. Kelly, S.D.; Hesterberg, D.; Ravel, B. Analysis of Soils and Minerals Using X-ray Absorption Spectroscopy. *Methods Soil Anal. Part 5 Miner. Methods* **2008**, *5*, 387–464.
80. Zabinsky, S.I.; Rehr, J.J.; Ankudinov, A.; Albers, R.C.; Eller, M.J. Multiple-Scattering Calculations of X-ray-Absorption Spectra. *Phys. Rev. B* **1995**, *52*, 2995. [CrossRef] [PubMed]
81. Hall, M.D.; Foran, G.J.; Zhang, M.; Beale, P.J.; Hambley, T.W. XANES Determination of the Platinum Oxidation State Distribution in Cancer Cells Treated with Platinum(IV) Anticancer Agents. *J. Am. Chem. Soc.* **2003**, *125*, 7524–7525. [CrossRef]
82. Grønvold, F.; Haraldsen, H.; Kjekshus, A. On the Sulfides, Selenides and Tellurides of Platinum. *Acta Chem. Scand* **1960**, *14*, 1879–1893. [CrossRef]
83. Tanley, S.W.M.; Schreurs, A.M.M.; Kroon-Batenburg, L.M.J.; Meredith, J.; Prendergast, R.; Walsh, D.; Bryant, P.; Levy, C.; Helliwell, J.R. Structural Studies of the Effect That Dimethyl Sulfoxide (DMSO) Has on Cisplatin and Carboplatin Binding to Histidine in a Protein. *Acta Crystallogr. D Biol. Crystallogr.* **2012**, *68*, 601–612. [CrossRef]
84. Williams, R.J.; Dillin, D.R.; Milligan, W.O. Structure Refinement of Potassium Chloroplatinate by Powder and Single-Crystal Methods. *Acta Crystallogr. B* **1973**, *29*, 1369–1372. [CrossRef]
85. Ohba, S.; Sato, S.; Saito, Y.; Ohshima, K.-I.; Harada, J. Electron-Density Distribution in Crystals of Potassium Tetrachloroplatinate(LI) and Influence of X-ray Diffuse Scattering. *Acta Crystallogr. B Struct. Sci.* **1983**, *39*, 49–53. [CrossRef]
86. Furuseth, S.; Selte, K.; Kjekshus, A. Redetermined Crystal Structures of $NiTe_2$ $PdTe_2$ PtS_2 $PtSe_2$ and $PtTe_2$. *Acta Chem. Scand* **1965**, *19*, 257. [CrossRef]
87. Rao, U.V. (Ed.) *Platinum Group Metals and Compounds*; Advances in Chemistry; American Chemical Society: Washington, DC, USA, 1971; Volume 98, ISBN 978-0-8412-0135-4.
88. Ochi, M.; Yamada, I.; Ohgushi, K.; Kusano, Y.; Mizumaki, M.; Takahashi, R.; Yagi, S.; Nishiyama, N.; Inoue, T.; Irifune, T. *B* -Site Deficiencies in *A* -Site-Ordered Perovskite $LaCu_3Pt_{3.75}O_{12}$. *Inorg. Chem.* **2013**, *52*, 3985–3989. [CrossRef] [PubMed]
89. Milburn, G.H.W.; Truter, M.R. The Crystal Structures of Cis- and Trans-Dichlorodiammineplatinum(II). *J. Chem. Soc. Inorg. Phys. Theor.* **1966**, 1609–1616. [CrossRef]
90. Jones, P.E.; Katz, L. The Crystal Structure of Ammonium Tris(Pentasulfido)Platinum(IV) Dihydrate. *Acta Crystallogr. B* **1969**, *25*, 745–753. [CrossRef]
91. Pokrovsky, O.S.; Pokrovski, G.S.; Feurtet-Mazel, A. A Structural Study of Cadmium Interaction with Aquatic Microorganisms. *Environ. Sci. Technol.* **2008**, *42*, 5527–5533. [CrossRef]
92. Teo, B.K. *EXAFS: Basic Principles and Data Analysis*; Springer Science & Business Media: Berlin/Heidelberg, Germany, 1986; Volume 9.

93. Munoz, M.; Argoul, P.; Farges, F. Continuous Cauchy Wavelet Transform Analyses of EXAFS Spectra: A Qualitative Approach. *Am. Miner.* **2003**, *88*, 694–700. [CrossRef]
94. Zhihang, Y.; Liu, P. WtEXAFS [Code]. 2022. Available online: https://Github.Com/Himmelspol/WtEXAFS (accessed on 15 October 2022).
95. Pryadchenko, V.V.; Srabionyan, V.V.; Avakyan, L.A.; van Bokhoven, J.A.; Bugaev, L.A. Electronic Structure of Pt and Au Compounds Measured by X-ray Emission and X-ray Absorption Spectroscopies. *J. Phys. Chem. C* **2012**, *116*, 25790–25796. [CrossRef]
96. Laskar, C.; Bazarkina, E.F.; Kokh, M.A.; Hazemann, J.-L.; Vuilleumier, R.; Desmaele, E.; Pokrovski, G.S. Stability and Structure of Platinum Sulfide Complexes in Hydrothermal Fluids. *Geochim. Cosmochim. Acta* **2022**, *336*, 407–422. [CrossRef]
97. Asakura, H.; Kawamura, N.; Mizumaki, M.; Nitta, K.; Ishii, K.; Hosokawa, S.; Teramura, K.; Tanaka, T. A Feasibility Study of "Range-Extended" EXAFS Measurement at the Pt L_3 -Edge of Pt/Al_2O_3 in the Presence of Au_2O_3. *J. Anal. Atomic Spectrom.* **2018**, *33*, 84–89. [CrossRef]
98. Kothari, M.; Jeon, Y.; Miller, D.N.; Pascui, A.E.; Kilmartin, J.; Wails, D.; Ramos, S.; Chadwick, A.; Irvine, J.T.S. Platinum Incorporation into Titanate Perovskites to Deliver Emergent Active and Stable Platinum Nanoparticles. *Nat. Chem.* **2021**, *13*, 677–682. [CrossRef] [PubMed]
99. Roy, M.; Gurman, S.J.; van Dorssen, G. The Amplitude Reduction Factor in EXAFS. *J. Phys. IV* **1997**, *7*, C2-151–C2-152. [CrossRef]
100. Kelly, S.D.; Bare, S.R.; Greenlay, N.; Azevedo, G.; Balasubramanian, M.; Barton, D.; Chattopadhyay, S.; Fakra, S.; Johannessen, B.; Newville, M.; et al. Comparison of EXAFS Foil Spectra from around the World. *J. Phys. Conf. Ser.* **2009**, *190*, 012032. [CrossRef]
101. Glatzel, P.; de Groot, F.M.F.; Manoilova, O.; Grandjean, D.; Weckhuysen, B.M.; Bergmann, U.; Barrea, R. Range-Extended EXAFS at the L Edge of Rare Earths Using High-Energy-Resolution Fluorescence Detection: A Study of La in LaOCl. *Phys. Rev. B* **2005**, *72*, 014117. [CrossRef]
102. Liu, W.; Etschmann, B.; Mei, Y.; Guan, Q.; Testemale, D.; Brugger, J. The Role of Sulfur in Molybdenum Transport in Hydrothermal Fluids: Insight from in Situ Synchrotron XAS Experiments and Molecular Dynamics Simulations. *Geochim. Cosmochim. Acta* **2020**, *290*, 162–179. [CrossRef]